General Disclaimer

One or more of the Following Statements may affect this Document

- This document has been reproduced from the best copy furnished by the organizational source. It is being released in the interest of making available as much information as possible.

- This document may contain data, which exceeds the sheet parameters. It was furnished in this condition by the organizational source and is the best copy available.

- This document may contain tone-on-tone or color graphs, charts and/or pictures, which have been reproduced in black and white.

- This document is paginated as submitted by the original source.

- Portions of this document are not fully legible due to the historical nature of some of the material. However, it is the best reproduction available from the original submission.

UNIVERSITY OF ILLINOIS
URBANA

AERONOMY REPORT NO. 114

AN IMPROVED ROCKET-BORNE ELECTRIC FIELD METER FOR THE MIDDLE ATMOSPHERE

by
D. L. Burton
L. G. Smith

July 1, 1984

Library of Congress ISSN 0568-0581

Aeronomy Laboratory
Department of Electrical and Computer Engineering
University of Illinois
Urbana, Illinois

Supported by
National Aeronautics and Space Administration

UILU-ENG-84-2502

A E R O N O M Y R E P O R T

N O. 114

AN IMPROVED ROCKET-BORNE ELECTRIC FIELD METER FOR THE MIDDLE ATMOSPHERE

by

D. L. Burton
L. G. Smith

July 1, 1984

Supported by
National Aeronautics
Space Administration
Grant NGR 14-005-181

Aeronomy Laboratory
Department of Electrical and
Computer Engineering
University of Illinois
Urbana, Illinois

ABSTRACT

This report presents improvements in a rocket-borne electric field meter designed to measure the atmosphere's electric field and conductivity in the middle atmosphere. The general background of the experiment is given followed by details of changes in the instrument and data-processing schemes. Calibration and testing procedures are documented together with suggestions for future work.

TABLE OF CONTENTS

LIST OF TABLES

LIST OF FIGURES

1. INTRODUCTION

1.1 Electric Fields in the Middle Atmosphere

In the lowest atmosphere under fair weather conditions there exists a vertical potential gradient of about 100 V/m. The atmosphere at low altitudes also has finite conductivity. The potential gradient and conductivity lead to the conclusion that there is a current flowing down through the atmosphere and into the ground. Direct measurements confirm the existence of the current.

The origin of this current was first explained by Wilson [1920]. He suggested thunderstorms as the electrical generators of a global atmospheric electric system. A diagram of this electric system is shown in Figure 1.1.

The electrical conductivity of the atmosphere increases with height. Two major factors are involved. One is the increase in mobility of the charged particles associated with the decrease of atmospheric (neutral) density. The other is the presence of free electrons above 60 km.

A high conductivity implies low values of electric field for a constant current. Theory predicts electric fields of about 2 mV/m at 60 km and about 2 μV/m at 70 km.

The acceptance of a global atmospheric electricity system has been complicated by recent observations of electric fields in the middle atmosphere which are greater than theory predicts.

Various investigators have reported results of rocket flights that indicate vertical electric fields in the middle atmosphere that are much greater than expected. Bragin et al. [1974] and Tyutin [1976] observed a maximum value of 14 V/m at an altitude of 57 km. Other observations supporting the existence of large electric fields have been reported by Hale and Crosky [1979], Hale et al. [1981], Pfaff et al. [1980], Maynard et al.

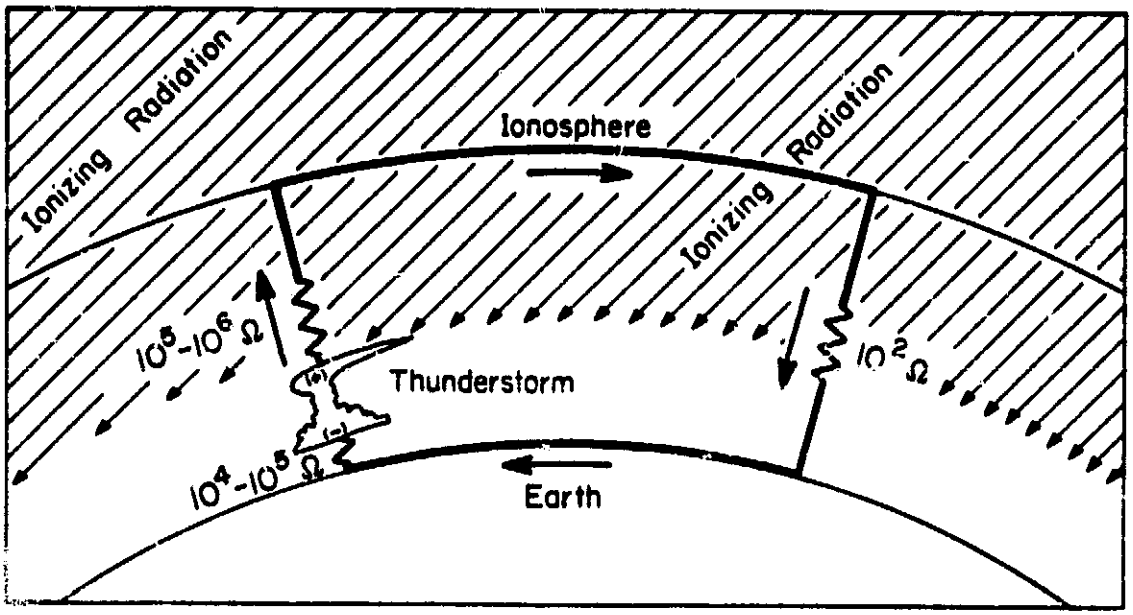

Figure 1.1 The atmospheric electrical global circuit. Large arrows indicate flow of positive charge. The thunderstorm depicted represents the global electrical generator, that is, the totality of all global thunderstorms. (Adapted from Markson [1978]).

[1981] and Maynard et al. [1982].

If these observations are accurate, the most obvious explanation is that it results from conductivity that is lower then expected, but low conductivity values are not supported by direct observations (Hale et al. [1981]). Kelley et al. [1983] suggest that large electric field observations have been artifacts of the experiments rather than actual ambient fields.

Two different types of instruments can be used to measure middle-atmosphere electric fields. If the conductivity is high enough a double floating probe, e.g., Mozer [1971], is effective. The potential difference between the two probes is measured using a high impedance voltmeter. The electric field value is derived from the voltmeter measurement and the known distance between the probes. If the conductivity is low, this method will not work without artificially increasing the conductivity near the probes. This is usually done with a radioactive source. This is not suitable for a rocket-borne measurement device in the lower part of the middle atmosphere.

In situations of low conductivity the preferred method of measurement uses electrostatic induction rather than electrical conduction. Instruments based on this principle are often called "field mills". These have been frequently and successfully used in studies of atmospheric electric fields in the low atmosphere. Adapting the technique for a rocket experiment in the middle atmosphere presents two major problems which are absent in ground-based measurements of the low atmosphere. These are: (1) the effects of atmospheric electrical conductivity (not negligible in the middle atmosphere) and (2) the constraints placed on the instrumentation resulting from the environment of the rocket in flight. These problems have been addressed in the design and construction of the electric field meter

described here.

1.2 An Induction Electric Field Meter

A rocket-borne field meter has been designed to measure the electric field and conductivity of the middle atmosphere and a prototype built, as described in Dettro and Smith [1982].

The electric field and the conduction current are both measured by separating the displacement component from the conduction component of the sensor current (the two components are in quadrature). The sensor consists of a conducting surface alternately covered and uncovered by a conducting shield. The area function of this surface is sinusoidal, resulting in a sinusoidally varying charge induced on the conductive sensor by the field and a sinusoidally varying current in the surface corresponding to the conductivity. A preamplifier converts the sensor current to a voltage.

The sensor output signal consists of two separate components. One represents the effect of conductivity and the other, 90 degrees out of phase, represents the electric field. The phase response of the system at the frequency of interest must also be known so that its effect can be compensated when separating the signal components. This includes the telemetry, pre-digitizing low-pass filter and data processing (digital filter and modulation detection) systems.

Previous designs of this type, e.g., Smith [1954], have been intended for use on the ground where fields are in the range of 100 to 10,000 V/m, and environmental conditions are not severe. In the case of Smith [1954], the experiment geometry resulted in an effective electric field intensification of ten times the ambient field (exposure factor = 10) so the meter sensitivity was actually 1000 V/m. Designing a field meter for use on a rocket is more difficult. The smallest field to be measured is 1 V/m, a

factor of 1000 less than the effective minimum field measured by Smith [1954], making noise problems much more significant. The rocket environment is also very harsh. High levels of vibration are present during launch. Acceleration forces will be in the range of 50 to 75 G. The rocket will spin at approximately 6 Hz throughout the flight putting a large stress on the mechanism.

The prototype instrument has successfully demonstrated the validity of the design. This report details changes in the instrument providing better reliability in flight with improved performance, and development of data processing schemes.

1.3 Plans For Rocket Launches

Two field meters are used to measure horizontal and vertical components of the electric field. One is mounted in the front of the rocket on the nose cone to measure the vertical field. The other is mounted in the side of the rocket to measure the horizontal field. Since the rocket is spinning, only one meter is required in the horizontal axis. This configuration is shown in Figure 1.2. The first rocket launch is mainly intended to be a test of the field meter so only the horizontal meter will be installed. (In any case the nose-tip position is not available on this flight.)

The field meter sensors must be exposed to the external field, therefore, the rocket nose cone must be ejected at a suitable altitude in order for the tip-mounted meter to operate. The side mounted meter will be exposed through a hole in the side of the rocket. The rotor will be protected from high wind velocities during launch by a deflector on the rocket just above the exposed meter.

The shape of the rocket will influence the ambient electric field. The effect is to increase the field near the rocket surface. The amount of

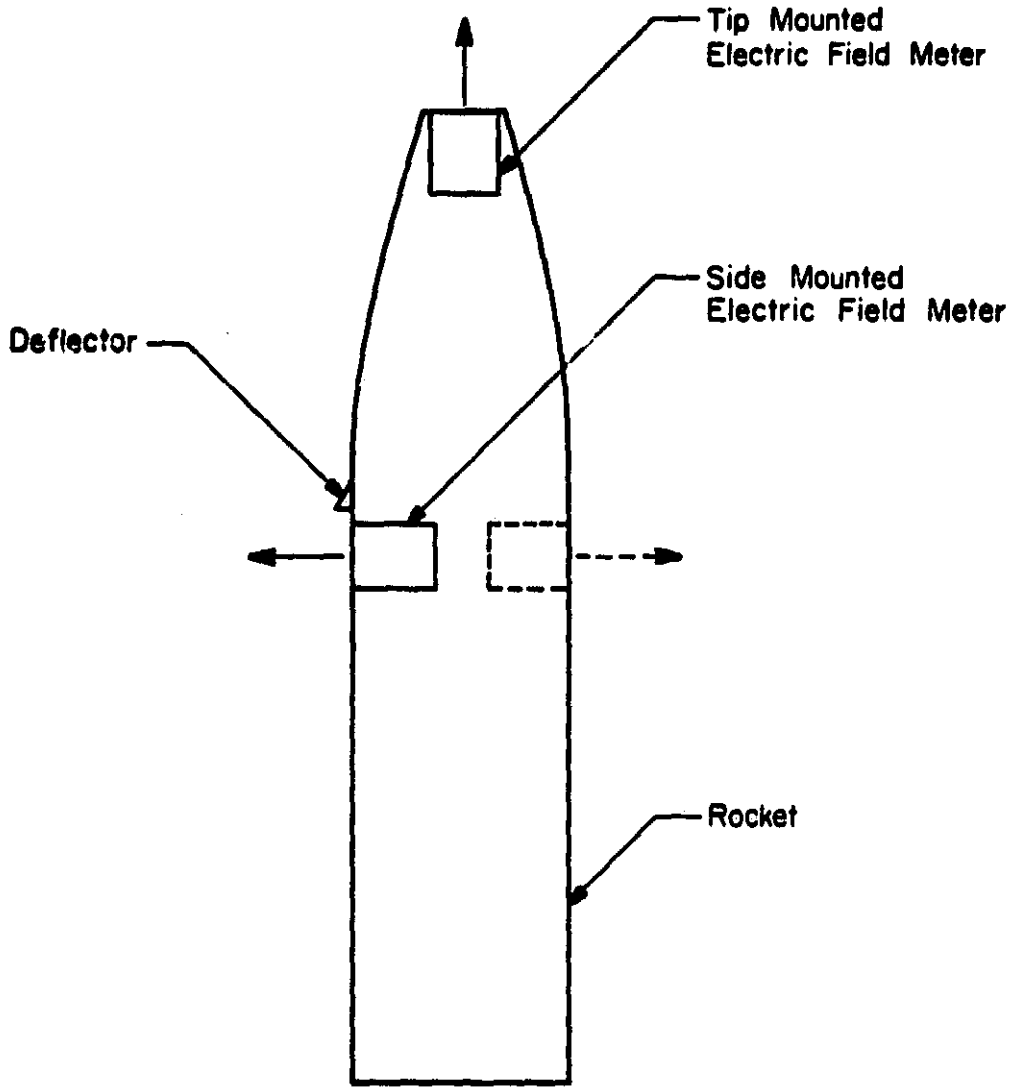

Figure 1.2 Suggested flight configuration using two electric field meters to measure the atmospheric electric field and conductivity. (Adapted from Dettro and Smith [1982]).

increase is specified as an exposure factor (Chalmers [1967]). As an example, the exposure factor of a sphere in a uniform electric field is three. The approximation for a rocket is an infinite cylinder. In this case the exposure factor for a perpendicular field is two. A better model for a rocket would be an ellipsoid, with exposure factor slightly greater than two at a point on the surface near the center of the major axis for a field perpendicular to the axis, and an exposure factor much greater than three at the end of the ellipsoid for a field in line with the major axis. The measured magnitude of the electric field must be divided by these factors to get the actual magnitude of the undisturbed field.

To obtain the best accuracy, a scale model of the rocket should be built and installed with electric field meters. A known electric field applied to the model would allow exact calibration of the two meter readings. For the system proposed here, the complete rocket could be exposed to normal (fair-weather) atmospheric electric field (about 100 V/m) and the exposure factor determined separately for the side- and forward-looking meters by suitably orienting the payload.

2. GENERAL CONSIDERATIONS

2.1 Modeling the Sensor

An electrical model of the sensor is required in order to design the signal processing electronic circuits and digital data processing algorithms. Figure 2.1 shows the sensor and rotor. When the rotor turns it alternately covers and uncovers the sensor surface. In the presence of an electric field this gives rise to an alternating current out of the sensor. Based on the theory given by Dettro and Smith [1982] an ideal sensor model can be constructed. This is shown in Figure 2.2.

This model consists of a voltage source representing the perpendicular component or the external electric field, a variable capacitor in series with the electric field source representing the rotor covering and uncovering the sensor, and a current source representing the conduction current into the sensor. The electric field source value is kE where E is the electric field strength and k is a constant. The modulating function of the variable capacitor is derived from the area function of the sensor as it is covered and uncovered by the rotor. C_o is the maximum value of the capacitor, corresponding to the sensor area being entirely exposed to the external electric field, ω is the rotor chopping frequency (200π rad/sec), and t is time. The capacitor gives the 90 degree phase shift to the electric field component of the sensor current. The conduction current source value is σkE, where σ is the conductivity, and is also modulated by the chopping frequency, $\sin\omega t$. The sensor is connected to the preamplifier input, which is a virtual ground.

This model suggests that in a non-conductive medium with no electric field the sensor current should be zero. In reality this is not the case. Tests show sensor current components at the chopping frequency and its

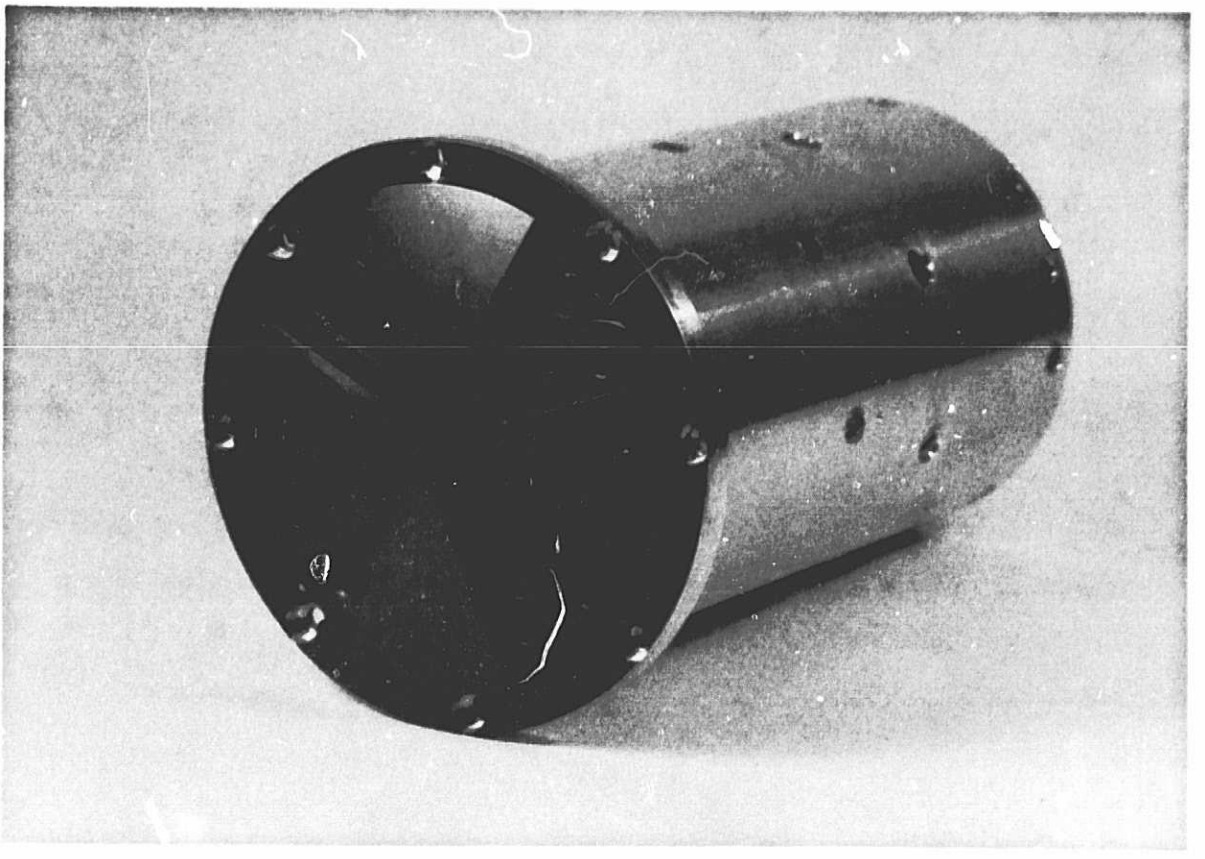

Figure 2.1 Electric field meter rotor and sensor.

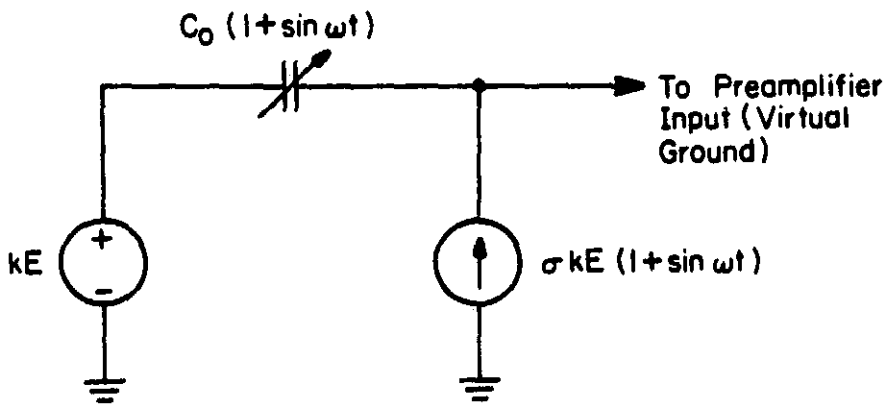

Figure 2.2 Ideal rotor-sensor model. (See text for explanation.)

harmonics. The origin of this "unwanted signal" is not well understood, but experiments show that uneven sensor and rotor surface work functions are at least part of the explanation. The magnitude of the unwanted signal can be reduced by coating all metallic surfaces in the rotor-stator area with colloidal graphite.

Another model taking into account the unwanted signal at the chopping frequency is shown in Figure 2.3. The unwanted signal is modeled by a second voltage source, V_1, with a variable capacitor , $C_1(\omega t)$, in series. The exact values of these additional components are not known other than the fact that rotor chopping action and work function are important. The rotor chopping action dependence is accounted for in the variable capacitor which varies as some function of the rotor frequency. This model may be further refined as a better understanding of the phenomenon emerges. Laboratory observations show unwanted signal levels corresponding to electric fields in the range of 4 to 13 V/m. The magnitude and waveform vary unreliably.

Data processing methods that separate the desired signal from the unwanted signal will be developed in Chapter 6.

2.2 Design of the Prototype

The prototype electric field meter described in Dettro and Smith [1982] was not intended to be launched on a rocket. It was intended to verify the design concepts in the laboratory and to provide the necessary data to design a version suitable for launch.

Mechanically, the prototype is not sound enough to withstand the vibration of a rocket launch or the centrifugal force of the rocket spin. Referring to Figure 2.4, the rotor blades are too thin. They would probably fatigue and break off during the high vibration of launch. The mechanical arrangement, shown in Figure 2.5, does not provide enough support to the

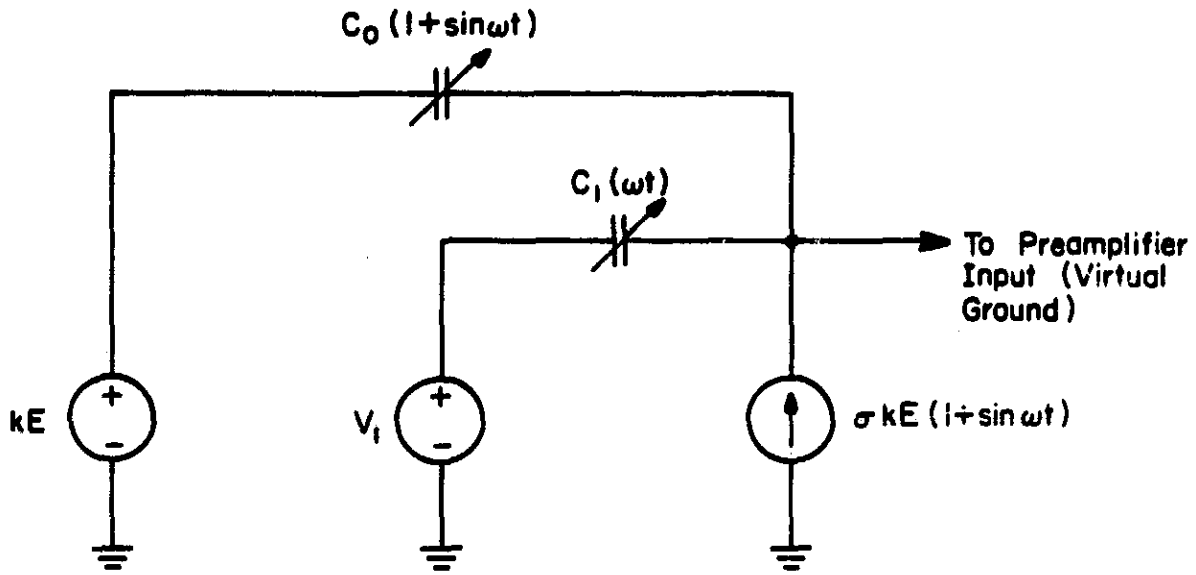

Figure 2.3 Actual rotor-sensor model. (See text for explanation.)

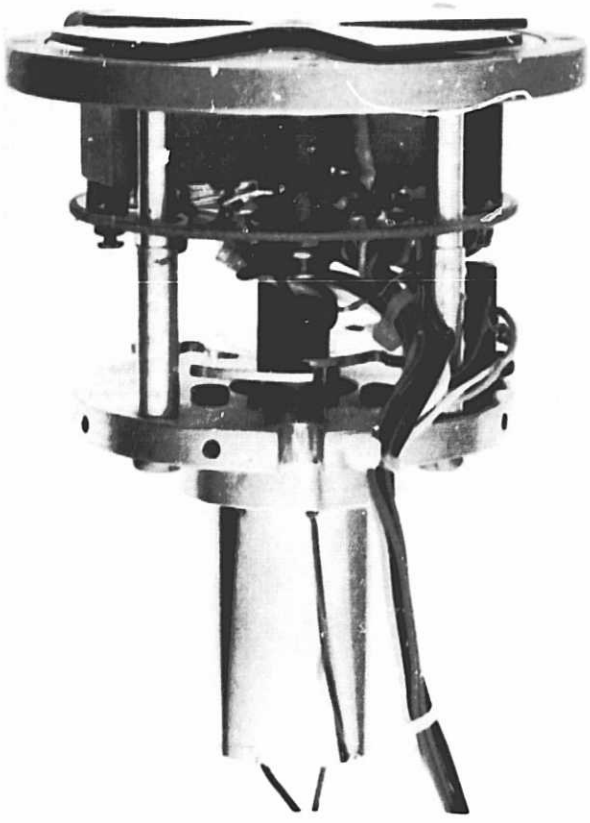

Figure 2.4 Prototype field meter with cover removed. (Dettro and Smith [1982]).

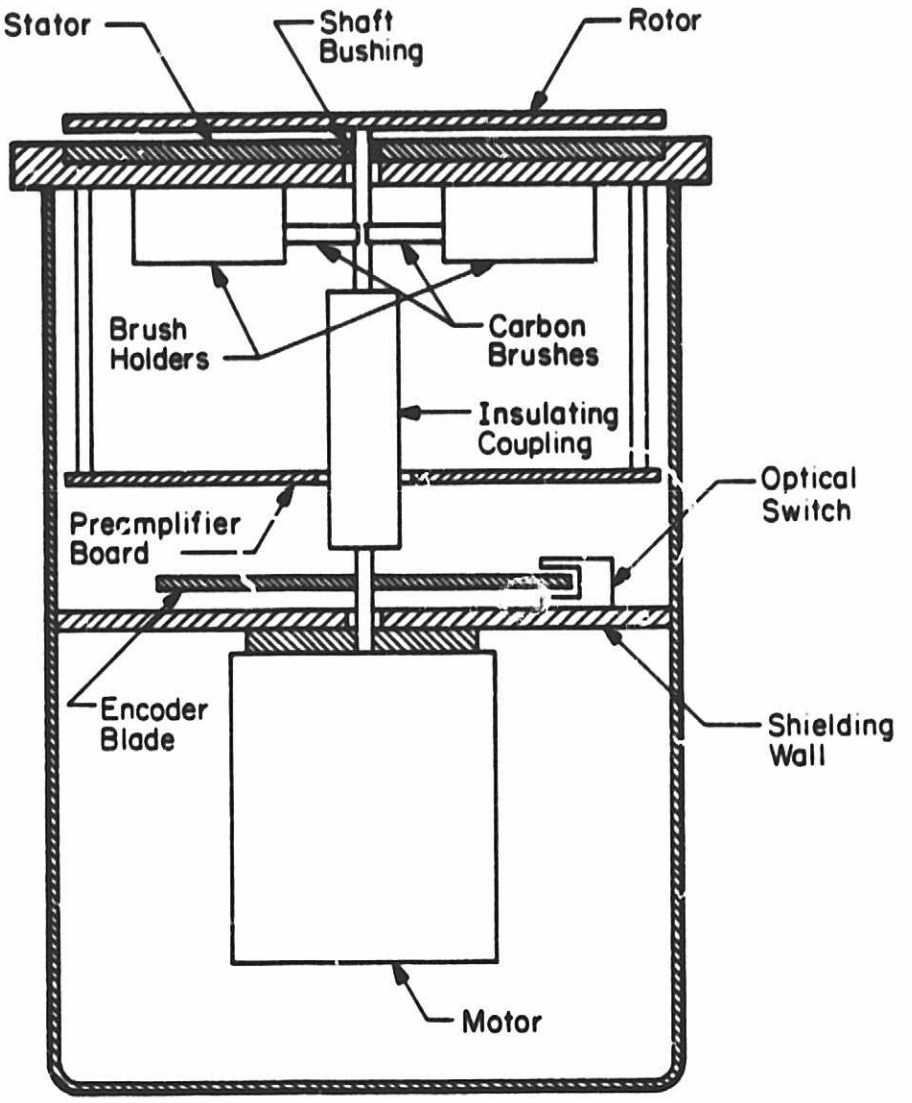

Figure 2.5 Mechanical arrangement of the prototype field meter. (Adapted from Dettro and Smith [1982]).

rotor shaft and the motor bearings. The rocket spin will cause a very large centrifugal thrust force throughout the flight. There is one shaft bearing just behind the rotor. The only other bearings are the built-in motor bearings. Another problem is motor and rotor shaft alignment. The solid coupling shown in the figure does not allow for any misalignment.

Carbon brushes are used in the prototype to ground the moving rotor. If the rotor is not continuously held at a constant potential with respect to the sensor, it will result in a noisy signal.

The block diagram of the prototype field meter is shown in Figure 2.6. The motor is a DC brush type. It is run open loop with speed set by a constant voltage regulator. DC brush motors have great speed variation with changes in load. The measured electric field amplitude is proportional to the motor speed and the proposed digital processing schemes (to be discussed later) require a constant motor speed so a closed loop control method is required.

The prototype preamplifier consisted of an op amp with a very large (1 GΩ) feedback resistor to the negative input. This large resistor couples with stray capacitance to give an unreliable frequency bandwidth to the preamplifier. It is also sensitive to stray leakage. Excessive resistor values must be reduced to no more than about 10 MΩ.

The prototype does a true RMS conversion of the signal to remove the rotor chopping frequency and then applies a logarithmic compression to improve the dynamic range. The log amplifier requires a temperature regulated cavity to maintain calibration and also limits the signal bandwidth.

A phase signal is generated from the rotor position encoder mounted on the rotor shaft. This phase signal allows separation of the electric field

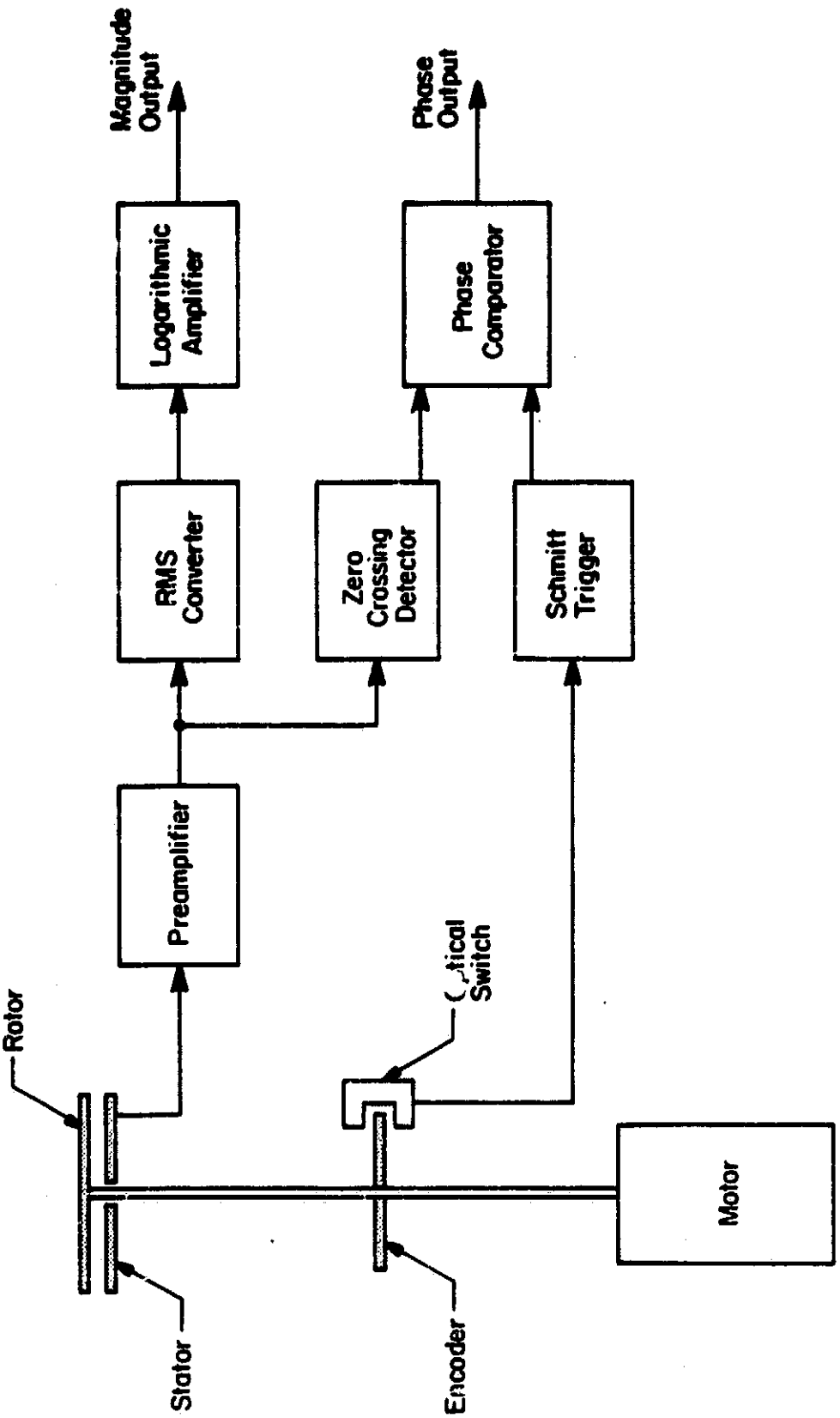

Figure 2.6 Block diagram of the prototype electric field meter. (Adapted from Dettro and Smith [1982]).

and conduction signal components.

2.3 Changes and Improvements

The new electric field meter design attempts to correct the problems of the prototype and also makes modifications as a result of new data processing ideas. The complete field meter system is shown in Figure 2.7.

The new rotor is thicker in the center where the blades are weaker and must endure the most stress, and tapers down towards the tips of the blades. The new rotor can be seen in Figure 2.1.

The mechanical arrangement of the improved meter is shown Figure 2.8. The rotor shaft is supported by a bronze bushing near the rotor providing lateral support and a ball bearing near the end of the rotor shaft providing lateral and axial support. The axial support provided by the ball bearing removes the thrust force from the motor bearings. The rotor shaft is connected to the motor through a special coupling which allows some alignment tolerance and isolates the shaft from motor vibration. The motor bearings only have to support the motor armature, the rotor position encoder and one half of the coupling. The encoder mass has been reduced to further minimize the motor bearing load.

The carbon brushes have been replaced by wire braid brushes and have been relocated in the encoder chamber rather than in the front deck.

The block diagram of the improved field meter is shown in Figure 2.9. The motor is still a DC brush type, but it has a built-in tachometer which is used to provide feedback to a closed-loop speed control. The motor and control circuit are identical to those used in many mini-floppy disc drives.

The RMS converter of the prototype has been deleted in favor of post-flight processing, which will extract the signal from the chopped sensor output. The log amplifier will not work at the rotor frequency so it is

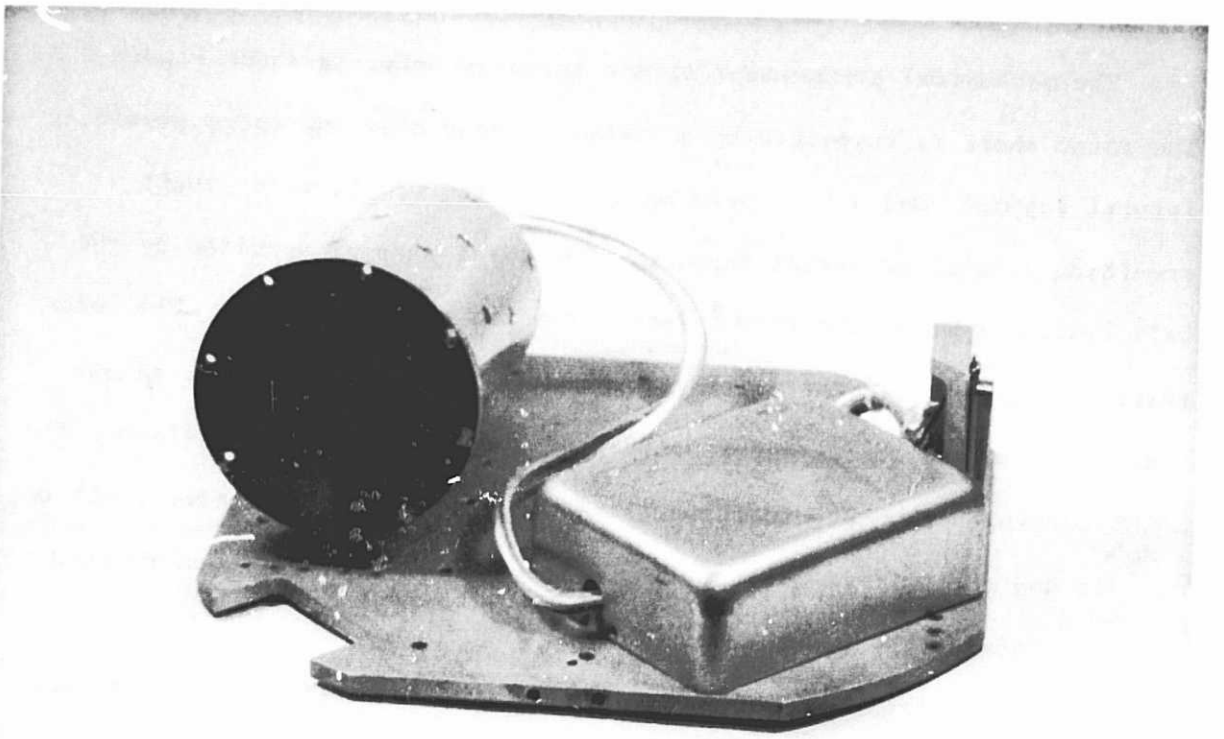

Figure 2.7 Complete electric field meter system.

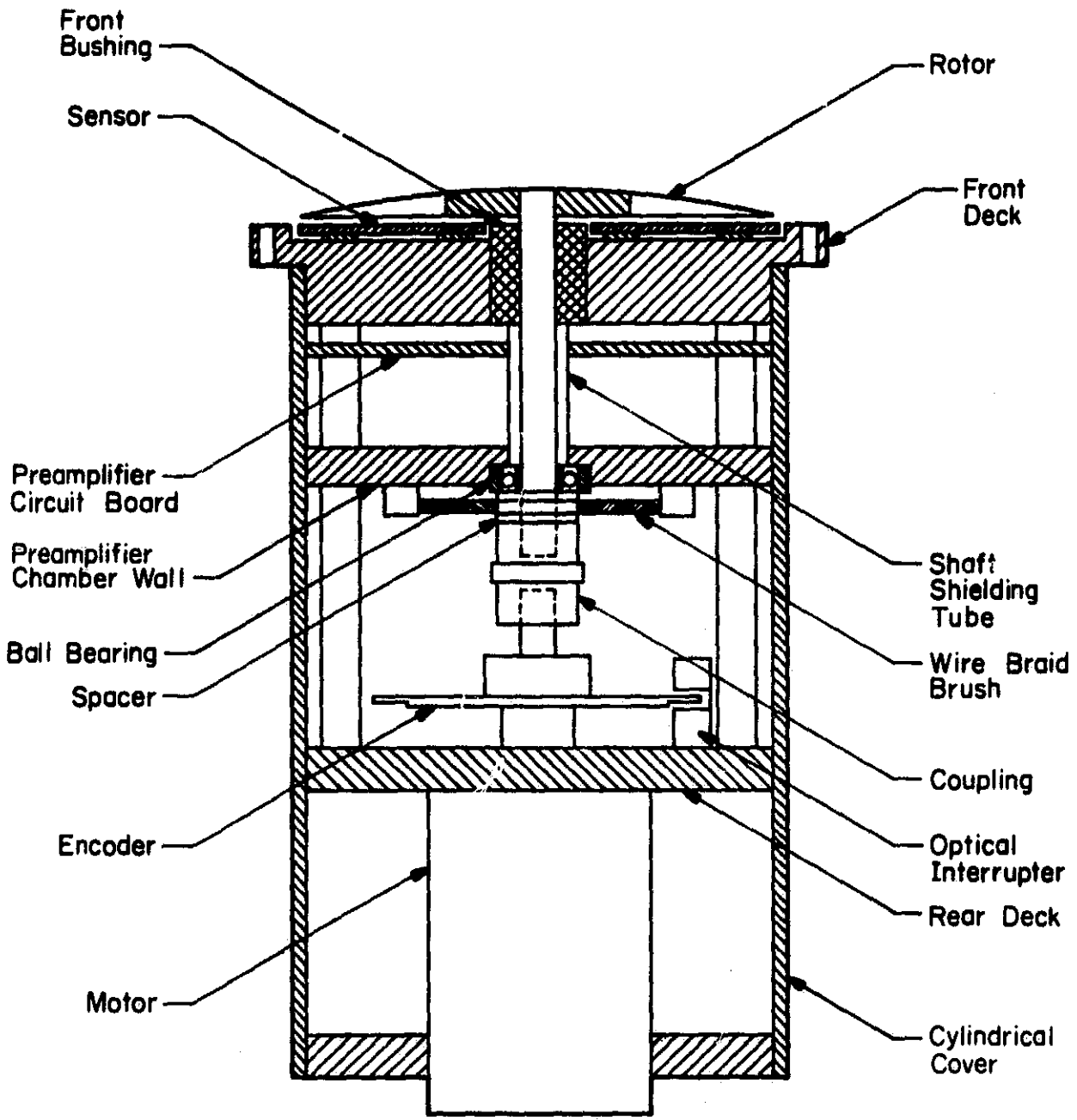

Figure 2.8 Mechanical arrangement of the improved electric field meter.

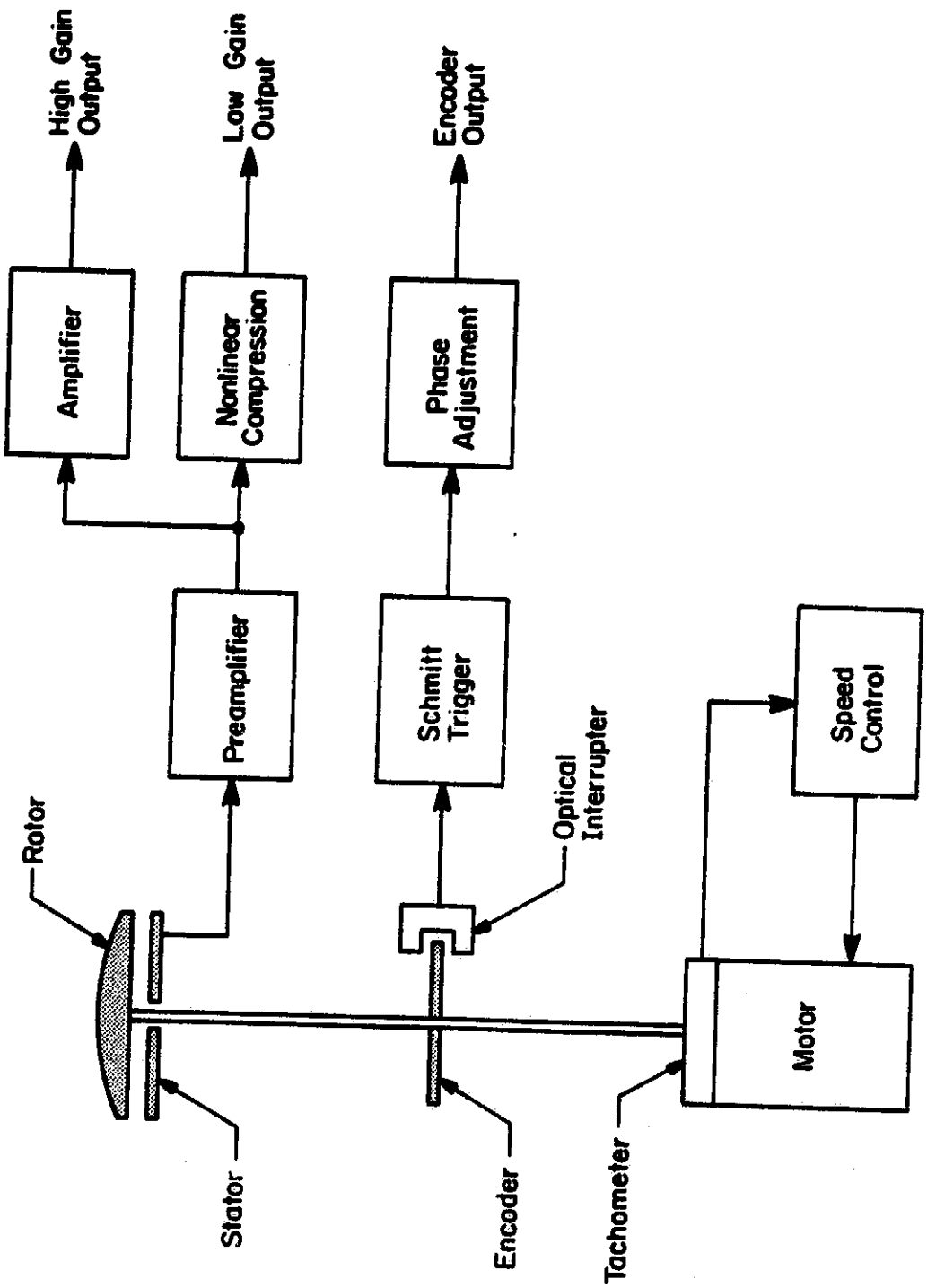

Figure 2.9 Block diagram of the improved electric field meter.

not used in the new field meter. A known nonlinearity is used for signal compression. The signal is reconstructed in post-flight processing. A high gain channel provides better resolution for low magnitude field measurements.

Rather than generate a phase signal in the meter to allow separation of the signal components, the encoder signal will itself be recorded for use in post-flight signal separation. It will also allow the motor speed variation (during the flight) to be studied.

Subsequent chapters will discuss the design of the improved field meter in detail.

3. ELECTRICAL DESIGN

3.1 Gain and Dynamic Range

There are two analog signal channels, one with high gain so that the maximum resolution for low-magnitude electric fields is obtained, and one with lower gain (and magnitude compression) so that high-magnitude electric fields can be measured without saturation of the telemetry channel.

There are many considerations to be made in setting the channel gains. The rocket telemetry system accepts signals in the range of 0 to 5 V, allowing a sinusoidal peak value of 2.5 V. The magnitude of the unwanted signal limits the maximum gain. The high gain channel is set to give a 4x amplitude margin (4x peak unwanted signal amplitude = 2.5 V) based on the laboratory attained unwanted signal magnitude. The low gain channel is set to give a good range overlap with the high gain channel. The high gain channel saturates at 50 V/m if the unwanted signal amplitude does not increase. Setting the low gain channel to give a 10% of capacity output (0.25 V) for a 20 V/m signal gives an ample channel overlap. The maximum field measurable is then determined by the preamplifier output voltage limits. This works out to be 1770 V/m. This value is reduced to 1000 V/m to give a good operating margin. The compression circuit to be discussed in Section 3.4 is adjusted to accommodate a 1000 V/m signal.

The resulting measurement ranges are 0 to 50 V/m on the high gain channel and 20 to 1000 V/m on the low gain channel.

3.2 Preamplifier Design and Noise Analysis

The desired measurement range is 1 to 1000 V/m. The peak sensor displacement current (I) is given by

$$I = 3.7 \times 10^{-12} E \qquad (3.1)$$

where E is the electric field magnitude (Dettro and Smith [1982]). By

laboratory measurement the sensor current resulting from a 1000 V/m electric field is 2.4×10^{-9} A. This experimental value modifies Equation (3.1) to be

$$I = 2.4 \times 10^{-12} E \ . \qquad (3.2)$$

This is 35% less sensor current than Equation (3.1) indicates. Considering the uncertainties of fringing loss and mechanical imprecision in the sensor, there is reasonable agreement between experiment and theory.

From Equation (3.2) a 1 V/m electric field gives a sensor current of 2.4 pA. In order to resolve this small of a current the preamp must have very high gain and very low noise. The preamplifier circuit is shown in Figure 3.1. It consists of a current-to-voltage converter, a non-inverting amplifier and a voltage follower. The first stage is the most critical. The sensor is connected to the negative input of the op amp (OA101). The output voltage is given by

$$V = -I \times (R101). \qquad (3.3)$$

To avoid leakage and bandwidth-limitation problems the value of R101 is limited to 10 MΩ. C101 is chosen to give a 300 Hz bandwidth to pass the desired 100 Hz signal and to limit higher frequencies. C101 significantly reduces the noise output of the current-to-voltage converter.

R106, R107, R108, C105, C106 and C107 implement an offset circuit with a range of 0.5 to -0.5 V. A portion of the unwanted sensor signal can be nulled out by adjustment of this offset. The actual effect is to force the rotor and sensor to slightly different potentials inducing a capacitive modulation signal as the rotor turns. This signal is out of phase with part of the unwanted signal allowing a nulling effect.

C102 and R102 block the DC component of OA101. If the DC was not blocked the high gain of OA102 would cause it to saturate. The value of

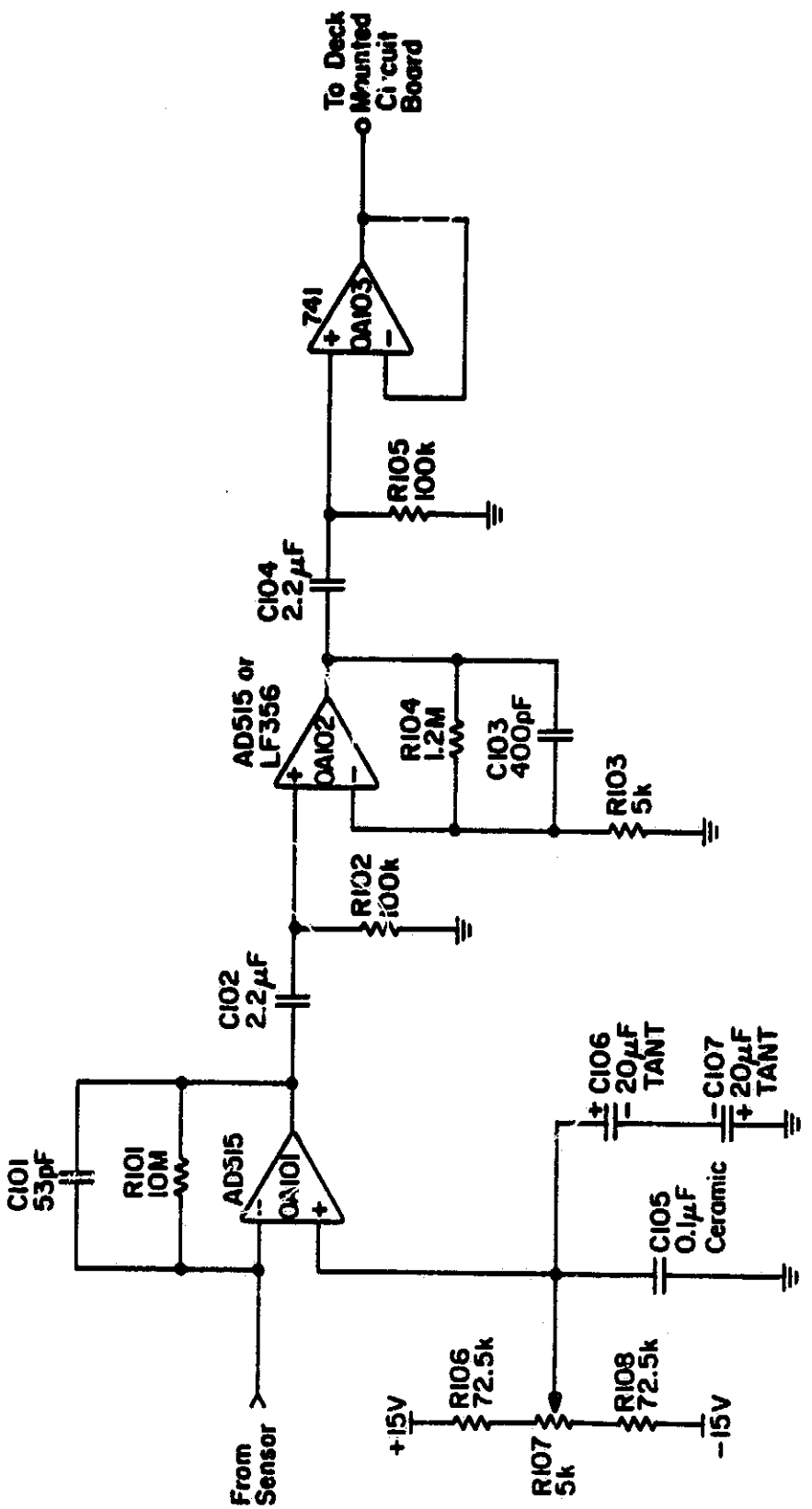

Figure 3.1 Preamplifier circuit diagram.

C102 is chosen to be as large as possible, limited by size, in an unpolarized capacitor. R102 forces the negative terminal of OA102 to settle to 0 V. It is chosen to give a settling time of about 1 second.

OA102 gives the second stage of gain. The non-inverting configuration is chosen so that the DC blocking circuit can have the high impedance load of the negative OA102 input to prevent signal amplitude loss. R103 and R104 are chosen to give a gain of 240 for reasons discussed in Section 3.1. This sets the overall gain of the low-gain stage. C103 is chosen to give the second stage a 300 Hz bandwidth.

C104 and R105 perform the same DC-blocking function as C102 and R102. OA103 is a voltage follower. It drives the shielded line connecting the field meter to the deck-mounted circuit board.

Since the gain of the first stage is so high (10^7 V/A), it is the most critical for low noise performance. The output voltage for a 1 V/m electric field is given by

$$V = 2.4 \times 10^{-12} \times 10^{7} = 24\ \mu V. \qquad (3.4)$$

The noise introduced by the electronics should be significantly less than this to allow detection of the desired signal.

The electronic noise model of the preamplifier first stage is given in Figure 3.2. The op amp input voltage and current, and resistive noise sources are included. The offset circuit is not included because the large values of C106 and C107 effectively ground the OA101 positive input for frequencies near 100 Hz. The noise sources can all be considered independent. By superposition, the output noise voltage is given by the root of the integral over the range of interest of the sum of the squares of the output noise voltage due to each source:

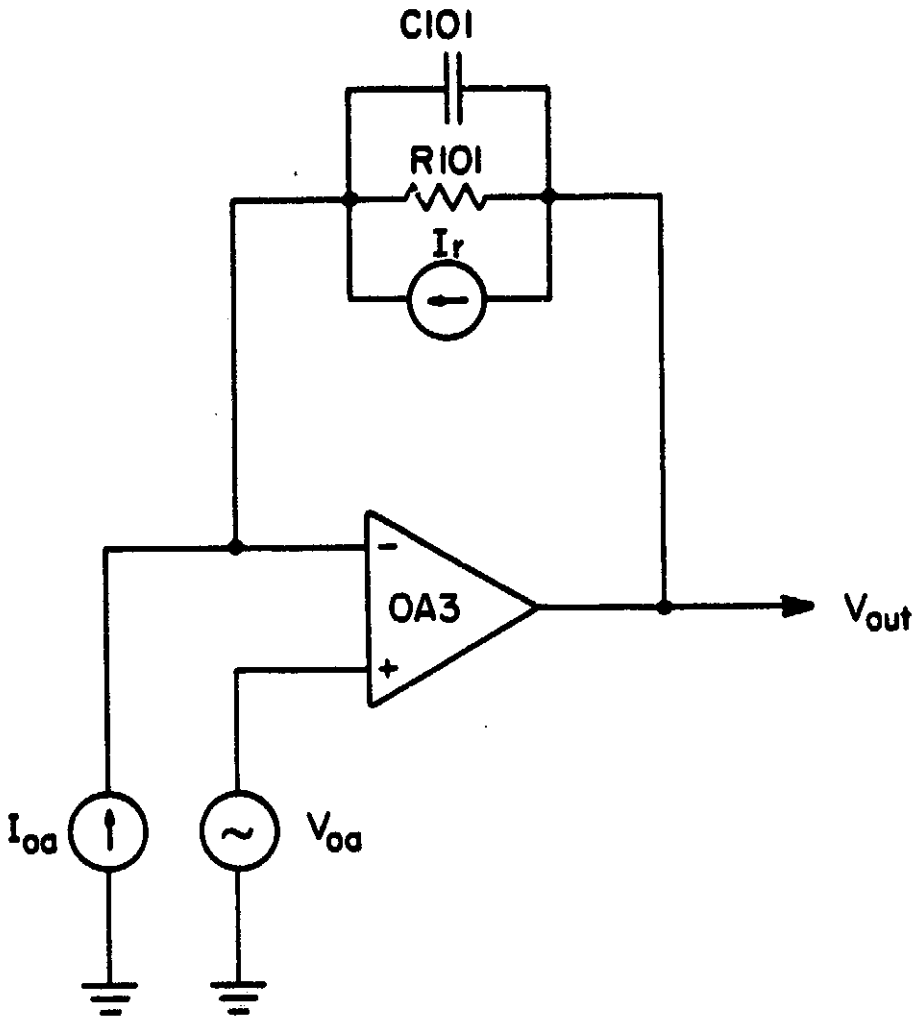

Figure 3.2 First gain stage electronic noise model.
(See text for explanation.)

$$V_{out} = \left\{ \int_{85}^{115} [(I_r^2 + I_{oa}^2) \left| \frac{R}{1 + SCR} \right|^2 + V_{oa}^2] df \right\}^{1/2} \qquad (3.5)$$

where I_{oa} and V_{oa} are the op amp input noise current and voltage spectral densities, and I_r is the feedback resistor noise current density given by

$$I_r = (4\ kT/R)^{1/2} \quad A/Hz^{1/2} \qquad (3.6)$$

where k is Boltzman's constant (1.38×10^{-23} J/K), T is the temperature and R and C are the values of R101 and C101. For T = 300 K and R = 10 MΩ:

$$I_r = 4.1 \times 10^{-14} \quad A/Hz^{1/2}. \qquad (3.7)$$

The range of integration is determined from the equivalent noise bandwidth (ENBW) of the post-flight processing digital filter. See Appendix II for the computation of the ENBW. The band is centered at 100 Hz.

An Analog Devices AD515J op amp has the following worst-case specifications:

Input voltage noise (V_{oa}): 20 $nV/Hz^{1/2}$

Input current noise (I_{oa}): 0.01 pA rms (10 Hz to 10 kHz)
(or 0.0001 $pA/Hz^{1/2}$).

The resulting OA1 output noise is 2.12 μV. If a more common type LF356 op amp with

Input voltage noise (V_{oa}): 20 $nV/Hz^{1/2}$

Input current noise (I_{oa}): 0.01 $pA/Hz^{1/2}$

is used, the resulting output noise is 2.18 μV.

Both of these noise levels are more than 20 dB below the 1 V/m signal amplitude so that either device is acceptable.

Experimental values for the electronic noise were obtained by digitizing the field meter output with the motor stopped and no external electric field. The digitized waveform was filtered with the digital band-

pass filter and the rms value of the waveform computed by taking the root of the sum of the squares of the time sequence samples. The result was 2.21 μV, in remarkable agreement with the calculated value.

3.3 Shielding

The preamplifier is very sensitive to pickup from stray electric and magnetic fields. During development of the improved field meter, large output signals were observed with no rotor attached and the sensor shielded from external electric fields. Further investigation determined the source of the signals to be coupling between the rotating rotor shaft, shaft coupling and position encoder and the preamplifier. There are 3 modes of coupling. The first is accomplished by a moving conductor modulating the ambient electric fields within the preamplifier compartment. The second is moving magnetized materials, e.g., set screws, coupling the preamplifier with a varying magnetic field. The third is moving nonconductors in the preamp compartment. Nonconducting material with charge trapped on the surface modulates the ambient electric field. As an example, the motor-to-rotor-shaft coupling was originally a phenolic cylinder with set screws to clamp the motor and rotor shafts. When a nylon set screw was used, an output signal of amplitude equivalent to an external electric field of 870 V/m was seen.

These problems were solved by shielding the preamplifier compartment from all moving parts. The mechanical design of the shield is covered in Section 4.4.

3.4 Compression, Amplifier and Offset Circuits

These circuits are shown in Figure 3.3. They are on the deck-mounted printed circuit board. The compression is a nonlinear function of the signal amplitude. If the diodes are considered to have ideal turn-on

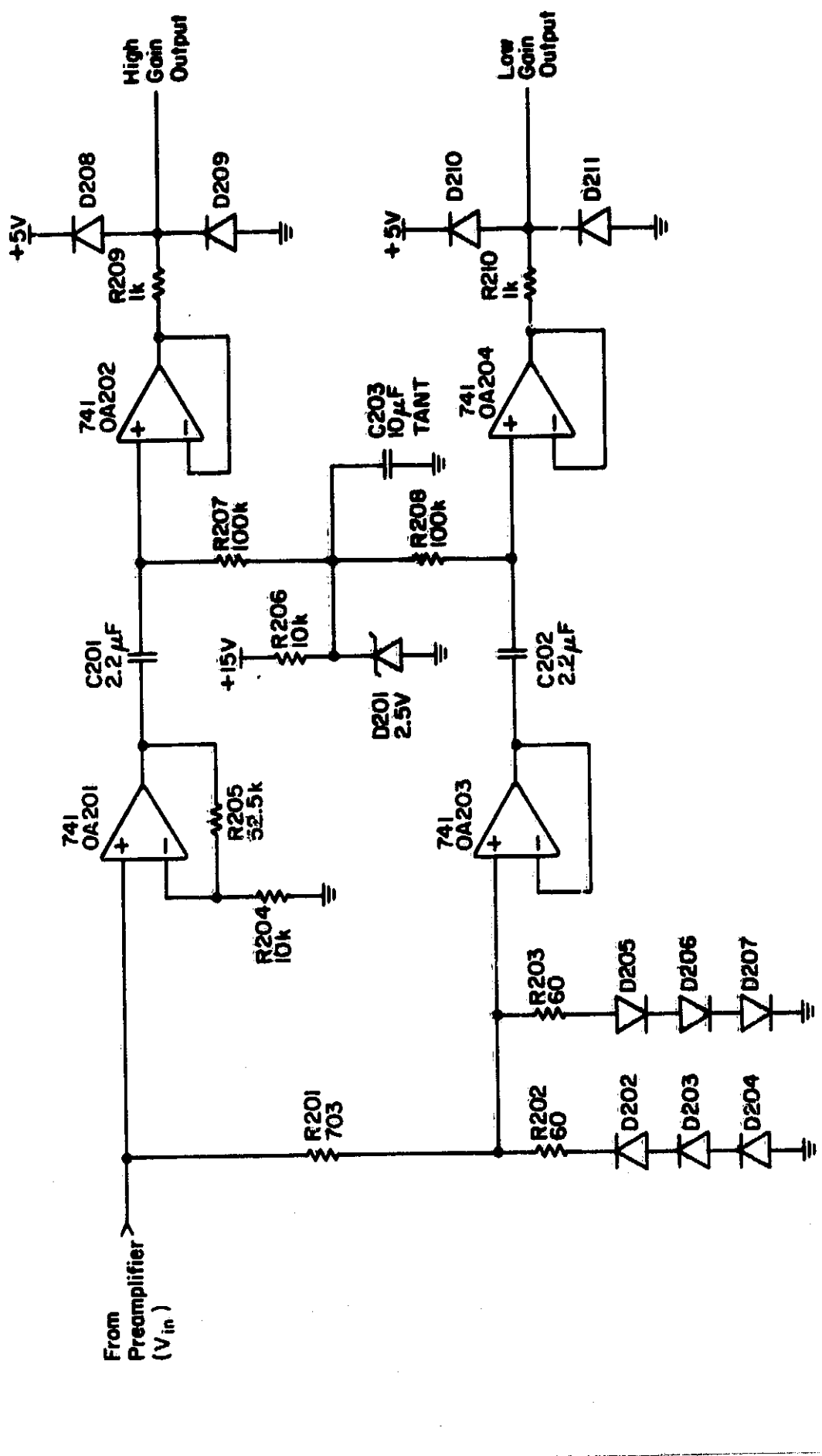

Figure 3.3 Circuit diagram of the amplifier, the non-linear compression and the offset.

points, then the compression can be described as having gain equal to one at amplitudes less than the diode turn-on points and as having a transfer function at amplitudes greater than the diode turn-on points given by

$$\text{Gain} = (R202 \times V_{in} + R201 \times V_d)/(R201 + R202) \qquad (3.8)$$

where V_d is the diode turn-on voltage. Non-ideal behavior is compensated for by characterizing the input-output transfer function and using this characterization to restore the signal. This is described more fully in Section 5.4.

The values of R201 and R202 are selected to draw a maximum current out of the op amp driving the circuit (OA103) and to give a maximum peak output voltage of 2.5 V for a 1000 V/m electric field. The diodes are selected to give a turn-on voltage at the desired compression break point.

The gains of the previous stages are adjusted to give a peak signal amplitude of about 0.25 V for an 20 V/m field (see Section 3.1). The compression break point is arbitrarily selected to be at about 300 V/m. At 300 V/m the measured value of V_{in} is 1.8 V. The diodes (D202 through D207) are selected to give break points of 1.8 volts (measured at 0.5 mA current). The output of the compression circuit should be 2.5 V peak-to-peak when the largest electric field to be measured (1000 V/m) is present. The output of OA103 is 6.0 V peak for this field magnitude. To limit the load on OA103 to 5 mA the diode voltage drop must be known at this current. It is measured to be 2.2 V. Values of R201 and R202 must be such that

$$(6.0 - 2.2)/(R201 + R202) = 5 \text{ mA} \qquad (3.9)$$

and

$$(R202 \times 6.0 + R201 \times 2.2)/R201 + R202 = 2.5 \text{ V}. \qquad (3.10)$$

Solution of these equations gives R201 = 703 Ω and R202 = 60 Ω. R203 is set equal to R202. The compression circuit output is buffered by an

additional amp voltage follower (OA203).

The high-gain channel amplifier (OA201) is also driven by OA103. To give an arbitrary margin of safety in the event that the unwanted signal magnitude increases, the gain is adjusted such that 4 times the measured unwanted signal output magnitude is at 100% of the output range. This amount of gain puts an upper limit of about 50 V/m on the high gain channel before saturation. The gain is set by R204 and R205.

Since the telemetry system input range is 0 to 5 V, both signal channels must be offset by +2.5 V to be compatible. This is accomplished by DC blocking the offset voltage from the outputs of OA201 and OA203 with a capacitor and referencing the output side of the capacitor to a 2.5 V reference through a resistor. These capacitors and resistors are C201, R207, C202 and R208. Their values are chosen in the same manner as C102 and RC102 in Section 3.2. The reference diode (D201) is biased through a 10 kΩ resistor (R206) from the +15 V supply and bypassed with a 10 μF tantalum capacitor (C203) to filter out any noise. The offset circuits are again buffered through voltage follower op amps OA202 and OA204. The outputs of these op amps are limited to the -0.7 to +5.7 V range by R209, R210 and D208 thru D211 to protect the telemetry system from overloads.

3.5 Encoder Circuit

The encoder circuit is shown in Figure 3.4. The rotor shaft position encoder chops the optical interrupter (INT401) 4 times for each shaft revolution. The interrupts are spaced 90 degrees apart. The interrupter consists of a photo-diode and a photo-transistor. The diode is biased on by the +15 V supply through a 470 Ω resistor (R401). The collector of the photo-transistor is pulled up to +5 V through a 5.1 kΩ resistor (R211). The emitter is connected to ground. If the light from the photo-diode is

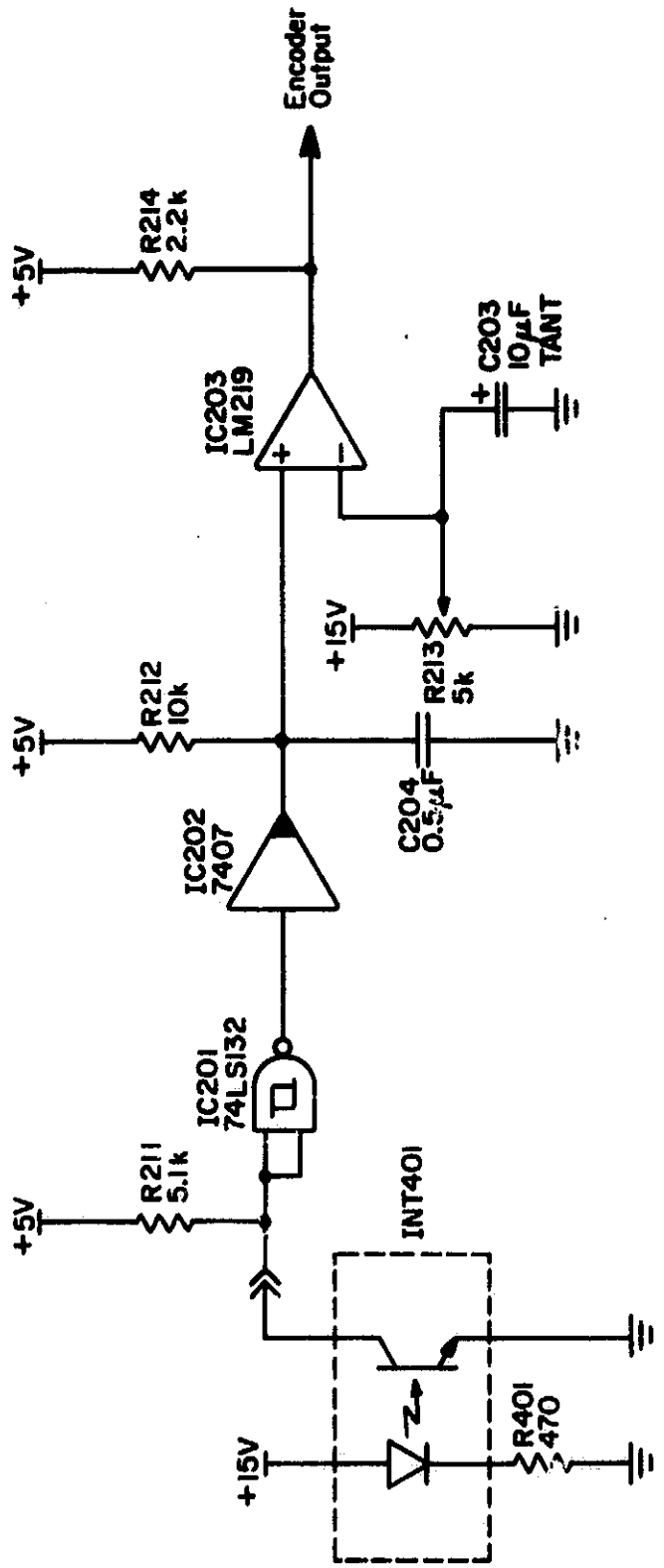

Figure 3.4 Encoder circuit.

allowed to reach the transistor, the transistor is turned on, pulling the collector voltage towards ground. If the photo-diode output is blocked by the position encoder, the transistor turns off allowing the collector voltage to be pulled up to 5 V.

The collector voltage is made into a clean and precise digital signal by a 74LS132 Schmitt trigger NAND gate (IC201). The output of the NAND gate drives a 7407 open collector buffer (IC202). The phase adjustment circuit is based on a circuit suggested by Dettro and Smith [1982]. It consists of an RC network on the output of the open collector buffer to allow a smooth-sloped rising waveform and a fast falling waveform, and a voltage comparator. The rising waveform is determined by the RC time constant, since the buffer output is off and the capacitor is charged from the +5 V supply through the resistor. The falling waveform is fast because the capacitor charge dumps into the buffer output transistor when it is on. The resistor (R212) and the capacitor (C204) values are selected to provide an adequate adjustment range for the phase calibration. The shaft rotational velocity is 25 Hz (40 ms per revolution). Since encoder pulses occur every 90 degrees, the maximum adjustment needed is 90 degrees, or 10 ms. Allowing for two RC time constants in 10 ms gives RC equal to 5 ms. This is realized by selecting R212 to be 10 kΩ and C204 to be 0.5 μF.

The resulting adjustment range is 81 degrees since the encoder blades are of finite width and the RC circuit is held low while the blades pass through the optical interrupter. If the adjustment range does not allow proper calibration of the encoder output, the encoder should be rotated 45 degrees with respect to the rotor in either direction.

The actual adjustment is accomplished by varying the reference voltage of the voltage comparator (IC203). The positive input of the comparator is connected to the capacitor (C204). The negative input is connected to the center tap of a potentiometer (R213). A 10 μF capacitor (C205) is connected between the center tap and ground for noise immunity. The potentiometer is connected between ground and +5 V allowing adjustment of the reference voltage over the same range. The output of the comparator is open collector and is pulled up to +5 V by a 2.2 kΩ resistor (R214). The comparator output goes directly to the telemetry system.

3.6 Motor Speed Control

The motor used to drive the rotor shaft is a DC brush motor with a built-in AC tachometer for feedback to the motor control circuit. The motor and the control circuit are virtually identical to those used in mini-floppy disk drives in the computer industry with the exception of a few minor modifications. The motors and control circuit were taken directly from the Hewlett Packard (Greeley Division) assembly lines. The motors are manufactured by Buehler and have Buehler part number 13.65.3.

The motor control circuit was modified to allow a slower motor speed, to operate from a different supply voltage (+15 and +28 V rather than +12 V), to fit on the deck mounted circuit board and to provide adequate power transistor heat sinking while operating in a vacuum. The supply that actually drives the motor is isolated from the payload +28 V supply by additional regulation through a +12 V IC voltage regulator.

The motor control circuit is shown in Figure 3.5. The heart of the circuit is IC204 which is the National Semiconductor LM2917 frequency-to-voltage converter including internal reference, op amp and output transistor. The 7.56 V internal reference diode is biased from the +15 V

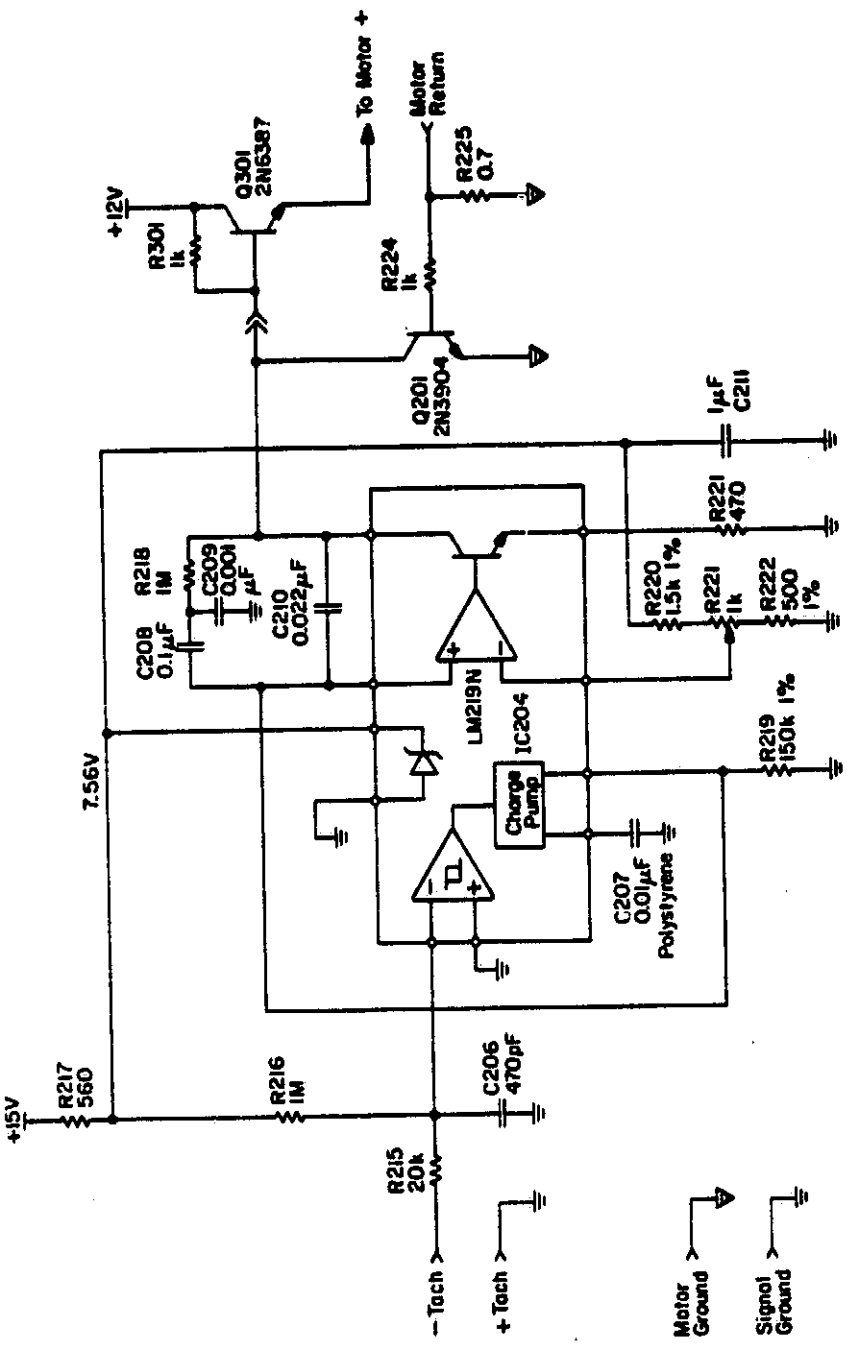

Figure 3.5 Motor control circuit.

supply through R217. The motor tachometer output drives the frequency-to-voltage converter through an RC low pass filter (R215 and C206). The frequency-to-voltage converter generates a DC voltage proportional to the motor speed.

C208, C209, C210 and R218 constitute the control loop filter. The IC204 compares the motor speed DC signal from the frequency-to-voltage converter with the speed reference voltage set by the motor speed adjustment circuit (R200, R211 and R222). The reference voltage is derived from the IC204 voltage reference. If the motor speed voltage is less than the reference voltage, the op amp decreases the base current of the output transistor. The motor-drive power transistor (Q301) is then turned on harder by the pullup resistor R301. The motor speeds up and the motor speed DC signal increases in turn.

If the motor is too fast, the motor speed DC signal will be greater than the speed reference voltage; the op amp will increase the output transistor base current which will result in more current being taken away from the base of Q301 reducing the Q301 emitter current and slowing down the motor.

R216 forces the control circuit to turn off the motor if there is no tachometer signal present. An additional transistor (Q201) turns on if the motor draws more than 1 A. This diverts the current from the base of Q301 limiting the maximum motor current to 1 A even under stall conditions. This is required to avoid an excessive drain on the payload battery should a stall or excessive load condition occur.

3.7 Power Requirements

The power distribution block diagram and the circuit of the power supply are shown in Figures 3.6a and 3.6b. All voltages are derived from the payload +28 and -28 V supplies. The +12 V supply for the motor is

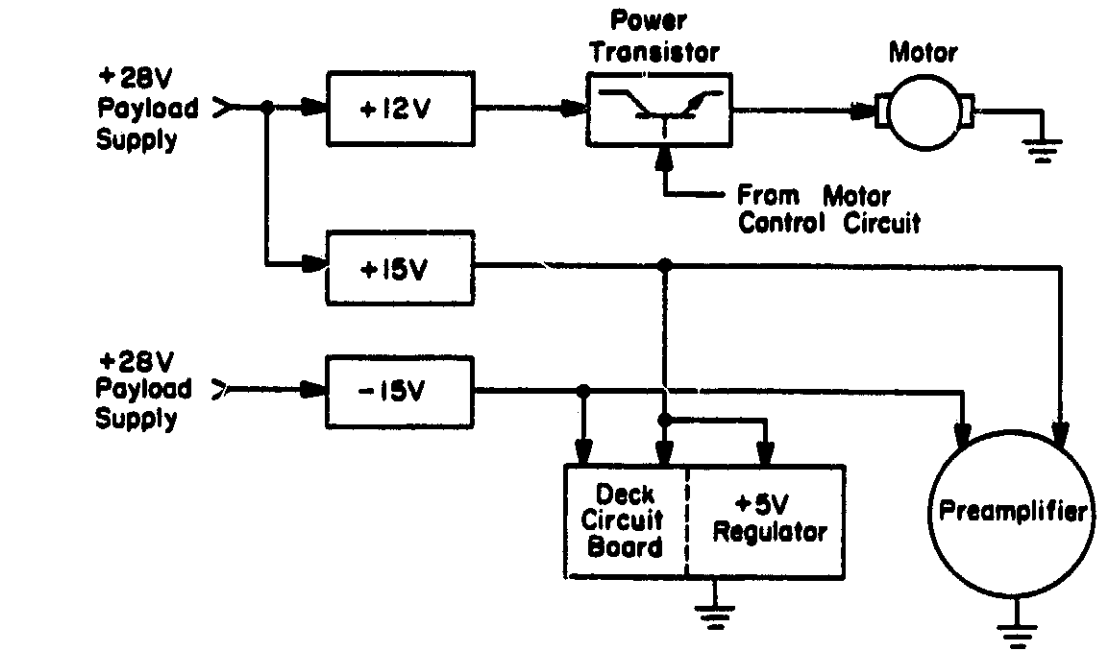

(a)

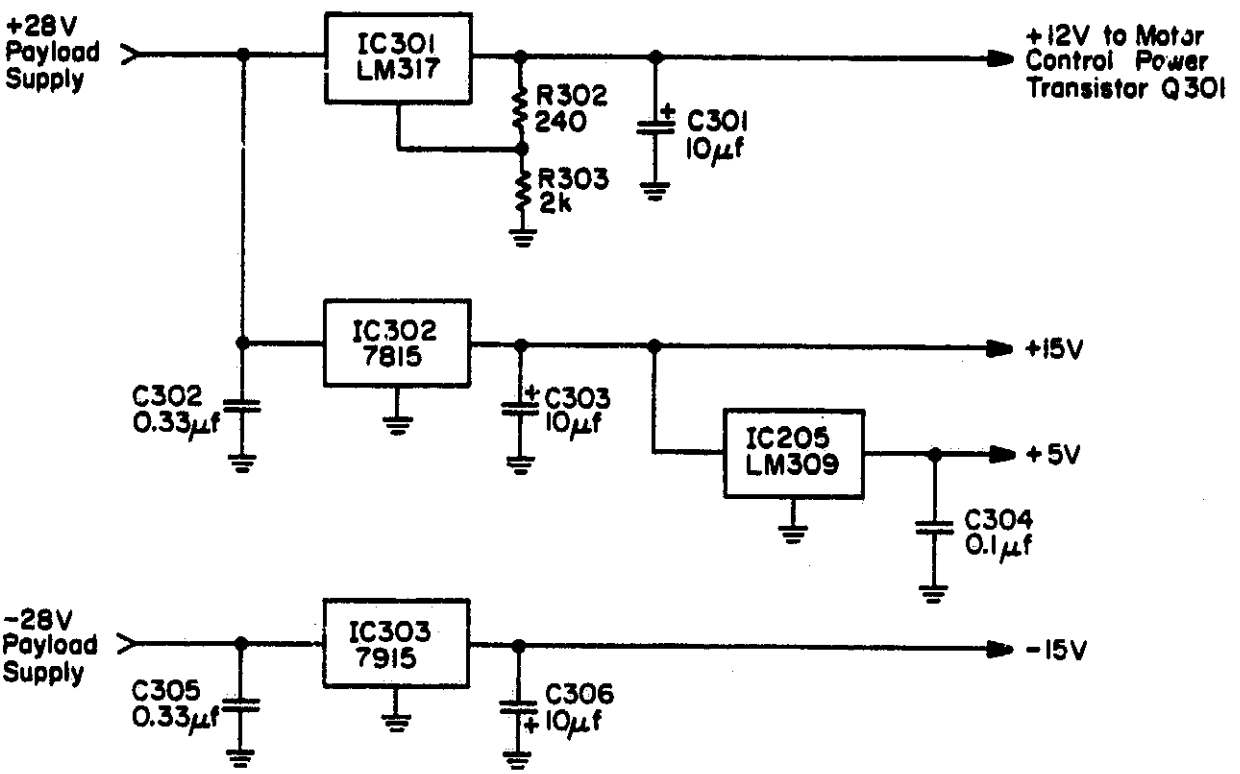

(b)

Figure 3.6 (a) Power distribution block diagram.
(b) Power supply circuit diagram.

obtained from the +28 V supply using an LM317 3-terminal adjustable regulator (IC301). R302 and R303 are chosen to set the output voltage to +12 V. The preamplifier and deck-mounted circuit boards use +15 and -15 V regulated down from +28 and -28 V by 7815 (IC302) and 7915 (IC303) 3-terminal IC voltage regulators. These are mounted on the aluminum deck below the deck-mounted circuit board together with the motor-control power transistor and the motor (+12 V) supply regulator. The deck-mounted circuit board also uses +5 V. This is generated on the board by an LM309 3-terminal IC regulator from the +15 V supply.

Power consumption of the electric field meter subassemblies is given in Table 3.1

Table 3.1 Electric field meter power consumption.

Motor	+12 V	300 mA typical, 1 A maximum
Preamplifier	+15 V	50 mA
	-15 V	15 mA
Deck-mounted circuit board	+15 V	70 mA (includes 40 mA for the + 5 V regulator)
	-15 V	10 mA
Overall payload supply loading	+28 V	420 mA typical, 1.12 A maximum
	-28 V	150 mA

4. MECHANICAL DESIGN

The mechanical arrangement of the field meter has been shown in Figure 2.8. A photograph of the meter with the cover removed is shown in Figure 4.1.

4.1 Motor and Drive Shaft

The motor is located in the rear of the instrument so that the preamplifier board can be mounted as close to the sensor as possible (to avoid noise pickup). The motor is connected to the rotor shaft through the encoder assembly (see Section 4.3) and the shaft coupling. The rotor is mounted on the end of the rotor shaft. The rotor shaft is supported at two points: at the front by a bushing and at the rear by a ball bearing. The rotor is prevented from touching the sensor by a 0.6 mm washer attached solidly to the rotor. The rotor-sensor gap is 1 mm (see Section 5.3) leaving 0.4 mm of play to allow for possible thermal expansion of the meter while in flight. If the washer is not firmly attached to the rotor, it will vibrate and introduce noise in the signal microphonically (see Section 6.4).

The shaft coupling has three parts, the shaft-side spline, the flexible ribbed ring and the encoder-side spline. The shaft-side spline set screws have been drilled out and replaced with larger ones. One extra is added to make three set screws on the shaft-side spline. This is required because these set screws hold the rotor and rotor shaft against the centrifugal force of the rocket spin.

The encoder-side spline is mounted on the encoder shaft and the ribbed ring installed between the two splines. The ribbed ring allows about 2 mm longitudinal freedom, 1.3 mm of lateral misalignment and 3 degrees of angular misalignment.

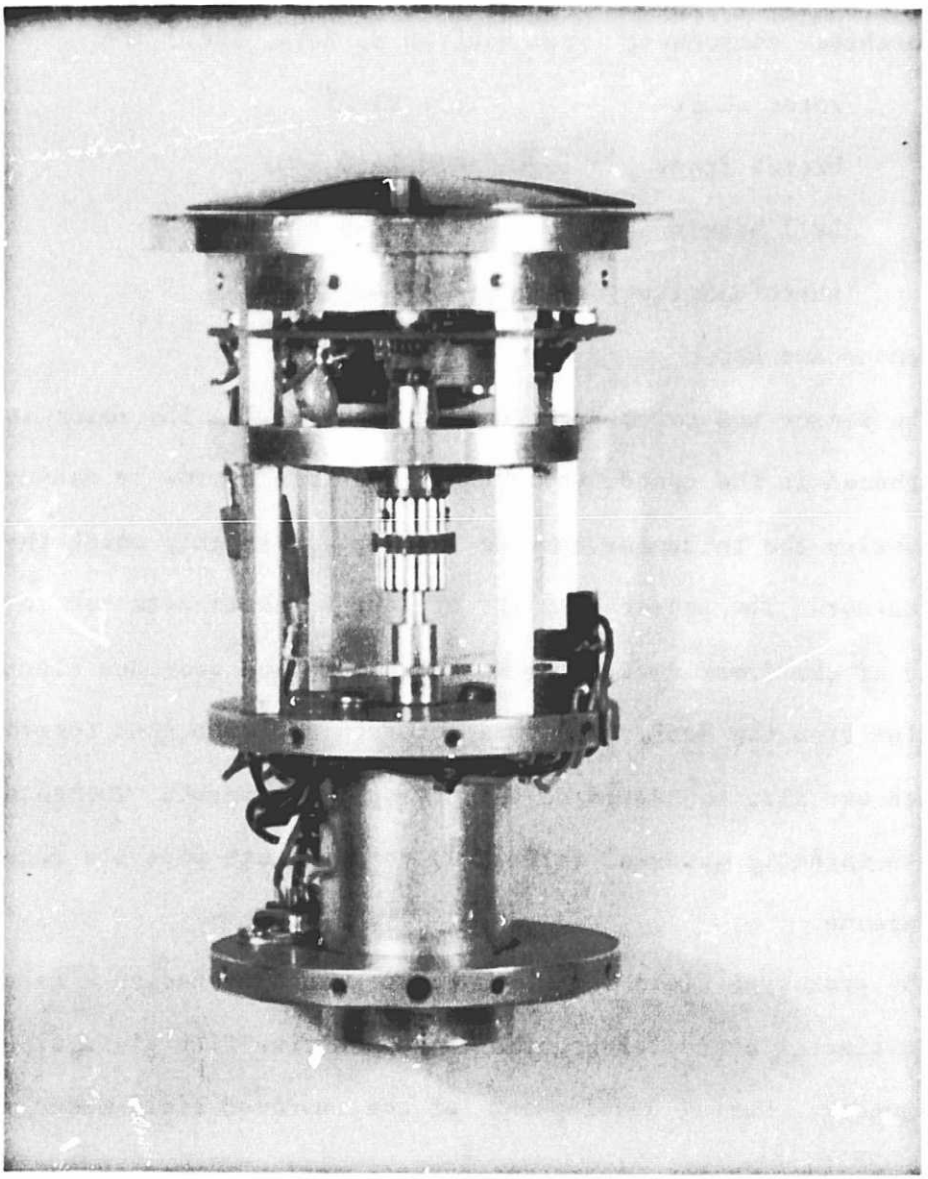

Figure 4.1 Field meter with cover removed.

The encoder is mounted on the motor shaft and the motor is secured to the rear deck. The motor bearings support the motor shaft, the encoder assembly and the encoder side of the coupling.

Purchased components (from Winfred M. Berg, Inc.) are:

rotor shaft	- # S3-23
bronze front bushings	- # B4-8
ball bearing	- # B2-6-S
shaft coupling assembly	- # CC9-20-3

4.2 Sensor and Rotor

The sensor and rotor are shown in Figure 2.1. The rotor is strengthened in the center where the blades are narrow by making it thicker and tapering the thickness towards the tips to roughly match the rocket body contour. The sensor consists of four segments attached to the outside surface of the front deck. The attachment method provides electrical isolation from the deck. The four segments are connected together behind the deck and also connected to the preamplifier input. The rotor is made of a non-magnetic material (aluminum) to eliminate possible magnetic field interference.

The prototype field meter had the segments etched on a fiberglass printed circuit board leaving the non-conductive fiberglass exposed between the segments. During development of the improved field meter, static charges trapped on the fiberglass surface were observed to influence the meter output. The new sensor design eliminates non-conductive material from the sensor area.

4.3 Encoder

The shaft angular position encoder blocks the optical interrupter four times for each shaft revolution, providing a pulse for each 90 degrees of

rotation. The encoder is machined from aluminum with an integral shaft on one side to attach the shaft coupler. The other side mounts on the motor shaft. See Figure 4.2.

4.4 Electrical Shielding

Section 3.3 discussed shielding required by the preamplifier circuit. This shielding is accomplished mechanically by a metallic tube enclosing the section of the rotor shaft passing through the preamplifier chamber and by the preamplifier chamber wall. The shaft fits into recesses in the front deck and chamber wall to provide a good electrical interlock. The preamplifier chamber wall provides shielding from the rotating coupling and encoder. The cylindrical field meter cover completes the preamplifier chamber shielding. The field meter with cover in place is visible in Figure 2.1.

4.5 Payload Installation

The field meter and electronics are shown mounted in a payload in Figure 4.3. The meter is shown in the approximate position it will occupy when the rocket shell is installed. The meter is attached to the 1/2 inch thick shell, not to the payload frame. The payload power supply is on the lower deck.

(a)

(b)

Figure 4.2 Encoder: (a) top view. (b) side view.

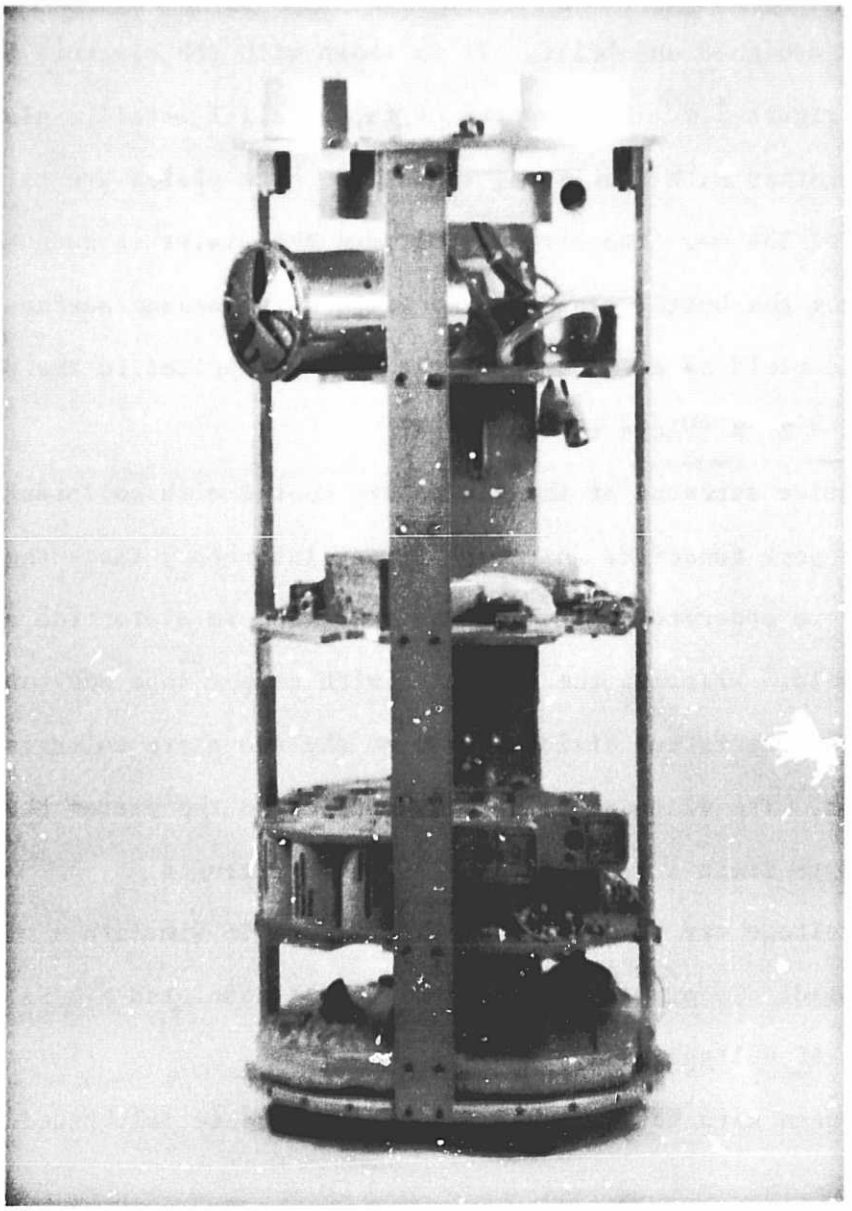

Figure 4.3 Payload installation.

5. CALIBRATION AND TESTING

5.1 Test Fixture for Electric Field Meter

In order to apply an external electric field to the meter a special fixture was designed and built. It is shown with the electric field meter mounted in Figure 5.1. It consists of two parallel metallic plates attached together with insulating standoffs. The plates are circular with a diameter of 254 mm. The distance between the plates is such that the distance from the bottom plate to the field meter sensor surface is 20 mm. The electric field as a function of the voltage applied to the plates is:

$$E = 50 \times (\text{Plate voltage}). \qquad (5.1)$$

The inside surfaces of the plates are coated with colloidal graphite to make the work functions uniform. During laboratory tests the insulating standoffs were observed to trap charge resulting in distortion of the electric field. Wrapping the standoffs with copper tape and connecting the copper tape to resistive dividers between the two plate voltages eliminated this problem. The external voltage is applied to the plates through a 10 kΩ resistor to limit current in case of short circuits.

A DC voltage may be applied to the fixture to simulate a constant electric field. To simulate an electric field modulated a 6 Hz rocket spin, a 6 Hz AC voltage is applied.

The system gain has been measured and the meter calibrated using this setup.

5.2 Motor Speed

The motor speed is adjusted by trimming the speed reference voltage potentiometer R221 described in Section 3.6. The location of R221 is shown in Figure 5.2. To obtain the proper adjustment for a 100 Hz rotor chopping frequency, a frequency counter is connected to the encoder output of the

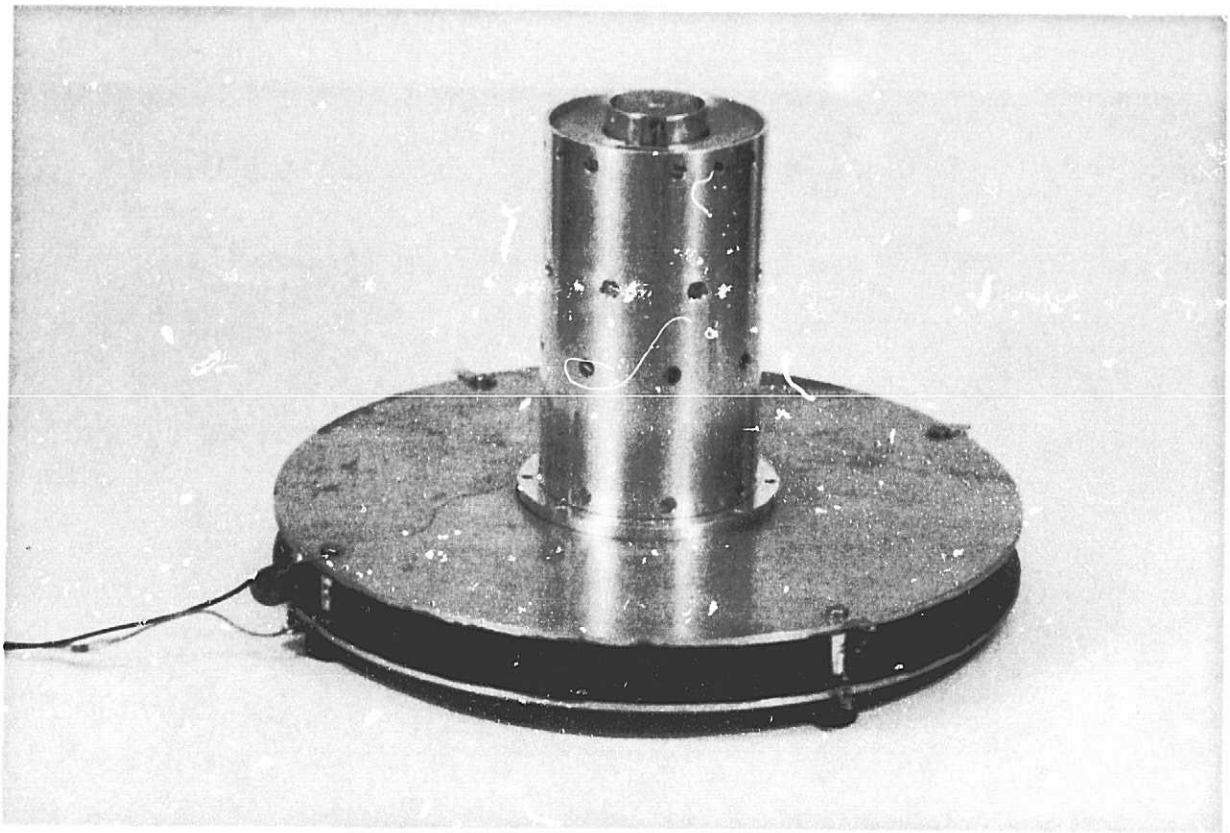

Figure 5.1 Test fixture for the electric field meter.

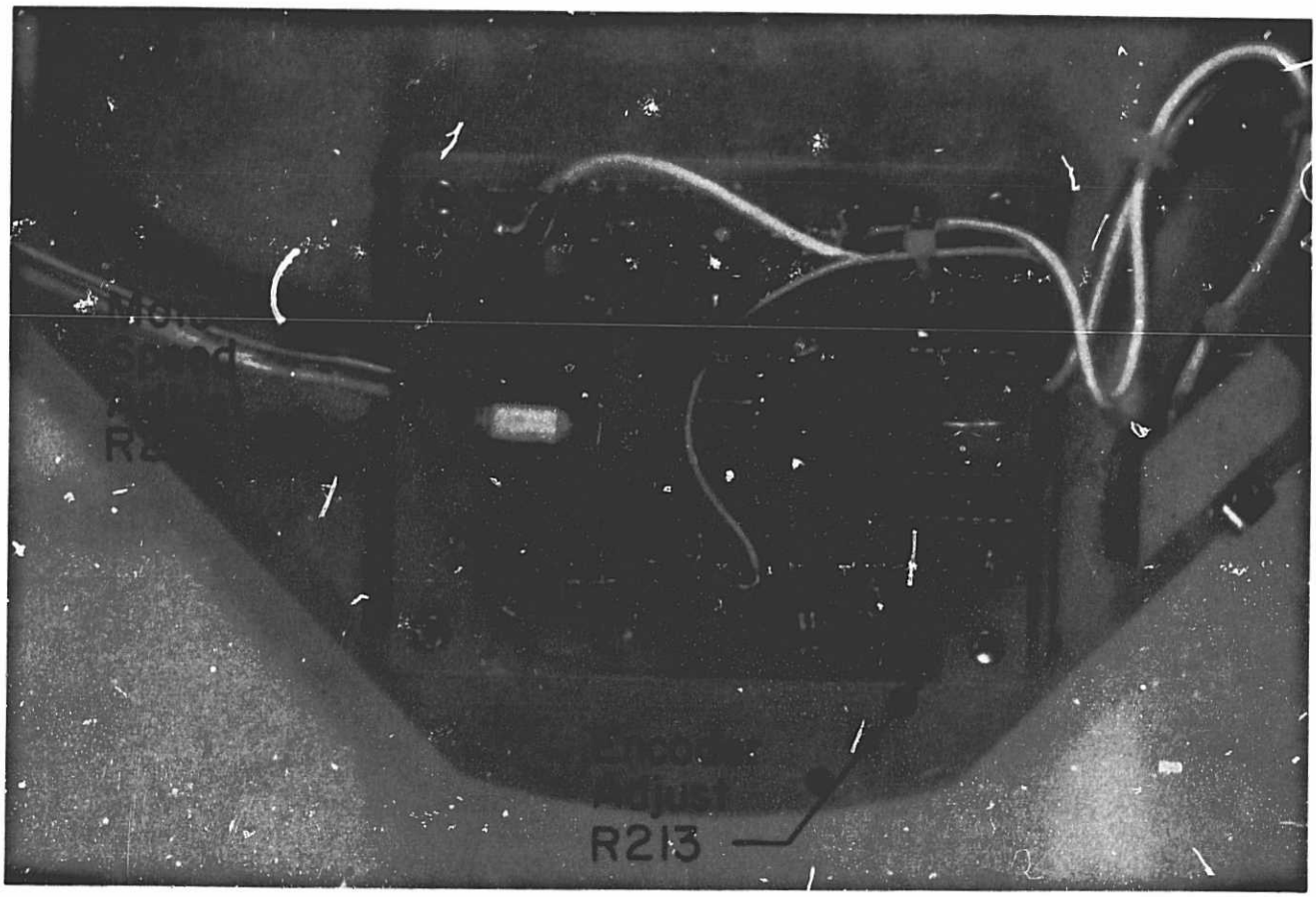

Figure 5.2 Deck-mounted printed-circuit board showing encoder and motor speed adjustment potentiometers.

field meter and the speed is adjusted to give a count of 100 Hz. If no encoder output signal is present, the encoder adjustment potentiometer should be turned until an output is obtained.

5.3 Rotor-Sensor Spacing

If the rotor-sensor spacing is too wide, the output (for a given electric field) will be diminished. If it is too narrow, the unwanted signal amplitude increases. By testing several gap widths, a gap of 1 mm was chosen as optimum. A tolerance of 0.1 mm is acceptable. The gap is obtained by stacking pages of a paper pad until the thickness is 1.0 mm. The pad is placed between a rotor blade and the sensor surface. Holding the rotor firmly against the paper and sensor, the rotor shaft side of the coupling is tightened onto the rotor shaft and the paper pad then removed from under the rotor blade. The gap spacing is maintained by the coupling position and the centrifugal outward force of the rocket spin.

5.4 Preamplifier Offset Adjustment

The unwanted signal from the field meter sensor can be reduced by adjustment of the DC potential of the sensor. The DC potential of the sensor is just the voltage offset of the first stage amplifier OA1. This is done by mounting a graphite coated end cap on the meter (see Figure 5.3) and trimming potentiometer R107 on the preamplifier circuit board to minimize the field meter OA103 output signal amplitude. The location of R107 is shown in Figure 5.4. Rotor and sensor should be coated with colloidal graphite and the rotor-sensor gap adjusted before attempting this.

5.5 Encoder Phase Adjustment

The encoder signal rising edge phase with respect to a pure electric field output (no conduction into sensor) must be known in order to separate

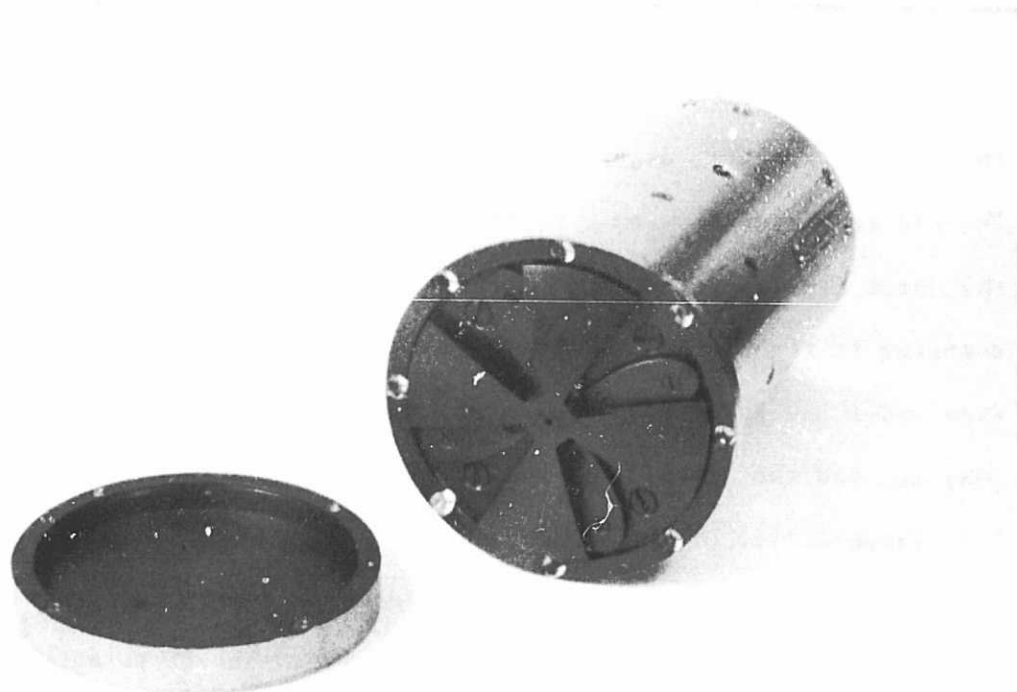

Figure 5.3 Electric field meter with end cap used to protec' rotor and sensor and to adjust preamplifier off .et.

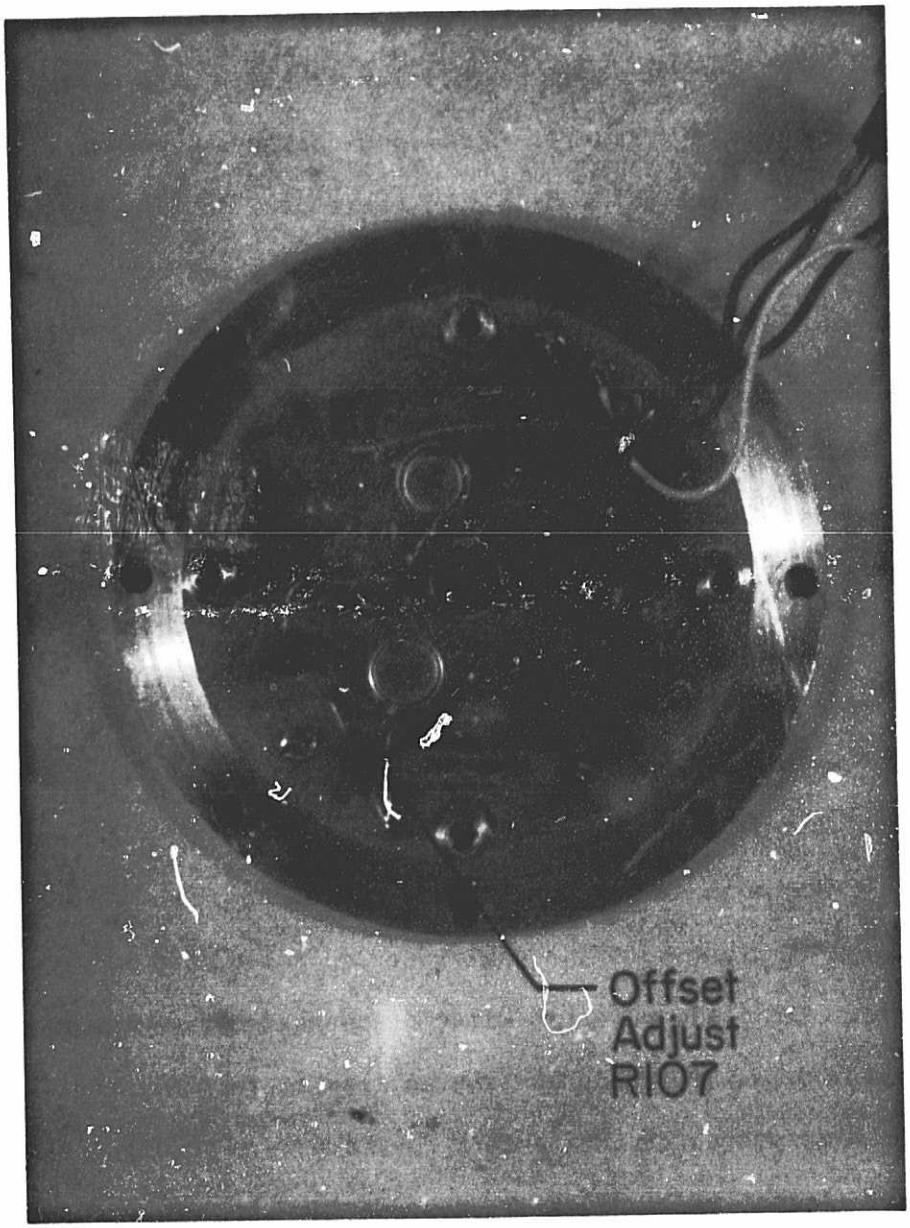

Figure 5.4 Preamplifier printed-circuit board showing offset adjustment potentiometer.

the electric field and the conduction signal components during post-flight processing. It is most convenient to align the encoder rising edge with the peak amplitude of a pure electric field output. To do this, mount the field meter on the electric field test fixture. Apply a large DC electric field (about 15 V on the fixture). While monitoring the output of OA103 and the phase output of IC203 with a dual trace oscilloscope, adjust potentiometer R213 to align the rising edge of the phase signal with the peak positive amplitude of the OA103 output. The location of R213 is shown in Figure 5.2.

5.6 Signal Compression Characterization

The compression circuit described in Section 3.4 is implemented with nonideal diodes resulting in a nonideal transfer function. In order to compensate for the nonideal behavior, the transfer function must be characterized. This is done simply by applying an input voltage and measuring the output voltage of OA203. The inverse of this function is applied during post-flight processing to restore the data.

There are many ways to automate this measurement. One simple way requiring only a ramp generator, a digitizer and a computer will be described here. The field meter is first disconnected from the deck-mounted circuit board. The ramp is then applied to the compression circuit. The compression circuit output waveform is next digitized at a high rate over the entire range of the compression circuit. If the digitizing rate is high, a fine characterization of the compression circuit is obtained by computing the difference between the compressed data sample values and the ramp input values for all samples. The ramp can be constructed mathematically because the sample values that are less than the non-linearity break points give the slope of the actual ramp. The results

of this characterization are shown in Figure 5.5.

5.7 Spin-Test Fixture

The field meter was spun at 6 Hz to determine if it would continue to operate and how much current the motor would draw. The special fixture shown in Figure 5.6 was built to do this. The fixture was mounted in an end mill and spun at 395, 500 and 680 rpm corresponding to spin frequencies of 6.58, 8.33 and 11.33 Hz. The motor current data at these spin rates are listed in Table 5.1. The radius of the fixture measured at the field meter rotor was 180 mm. This is slightly larger than the rocket radius. Power was provided to the motor control circuit and the encoder signal monitored through slip rings. The meter was tested with both a bronze bushing giving lateral and axial support and a ball bearing in the preamplifier chamber wall. There was much less drag with the ball bearing than there was with the bronze bushing.

5.8 Vacuum Testing

No problems were expected with operation for short periods in a vacuum, but a test was made to verify this. The field meter was mounted on the electric field test fixture in a vacuum chamber. The test fixture plate wires and field meter power and signal cables were brought out through an air-tight seal. The air pressure was reduced to the equivalent of more than 75,000 feet altitude for more than 30 min. No effect was observed on the f ld meter operation.

5.9 Vibration Testing

The field meter and all flight electronics will be vibration tested as a unit with the rest of the payload. As of the time of this report this had not yet been done.

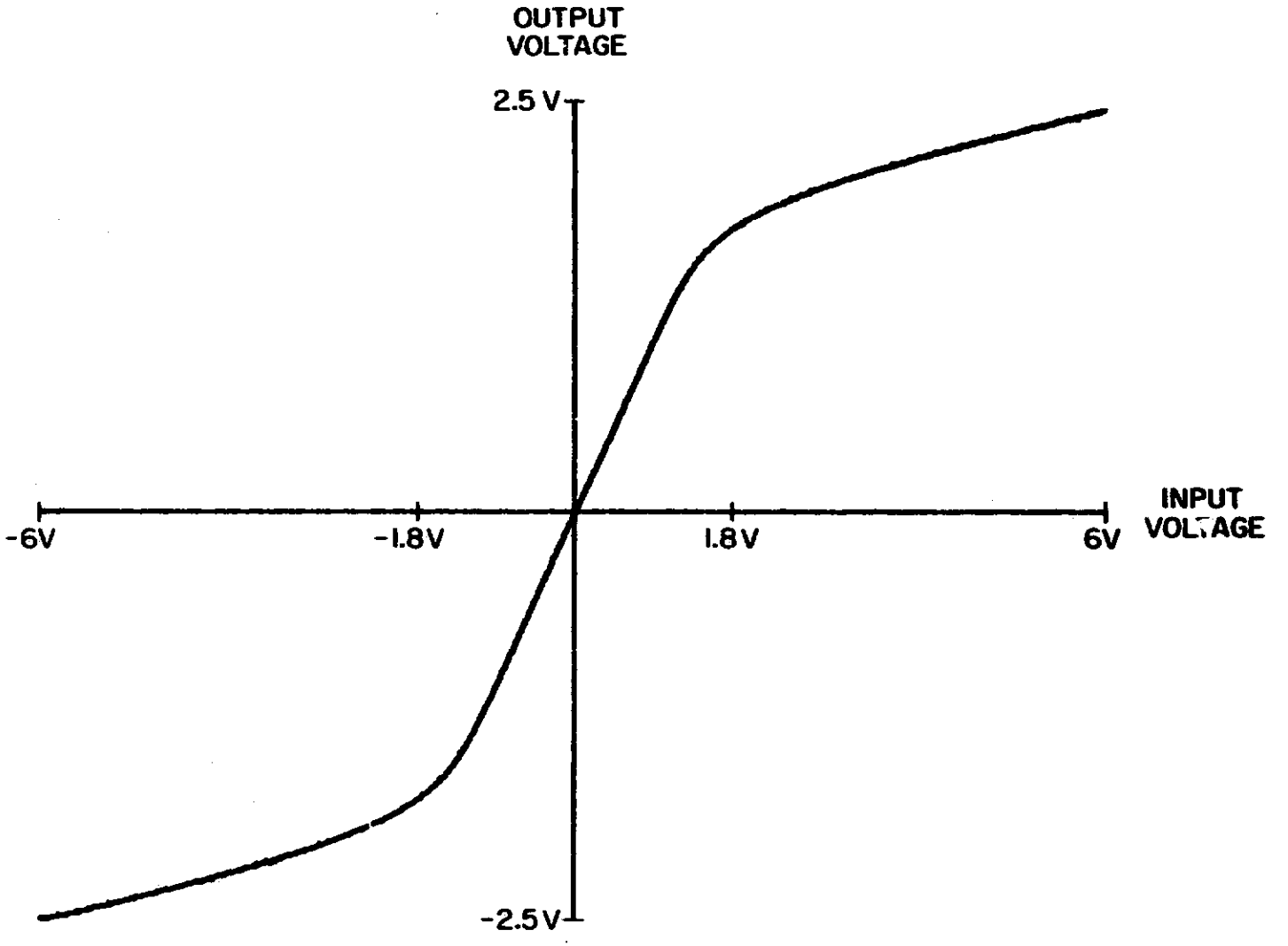

Figure 5.5 Compression characteristic.

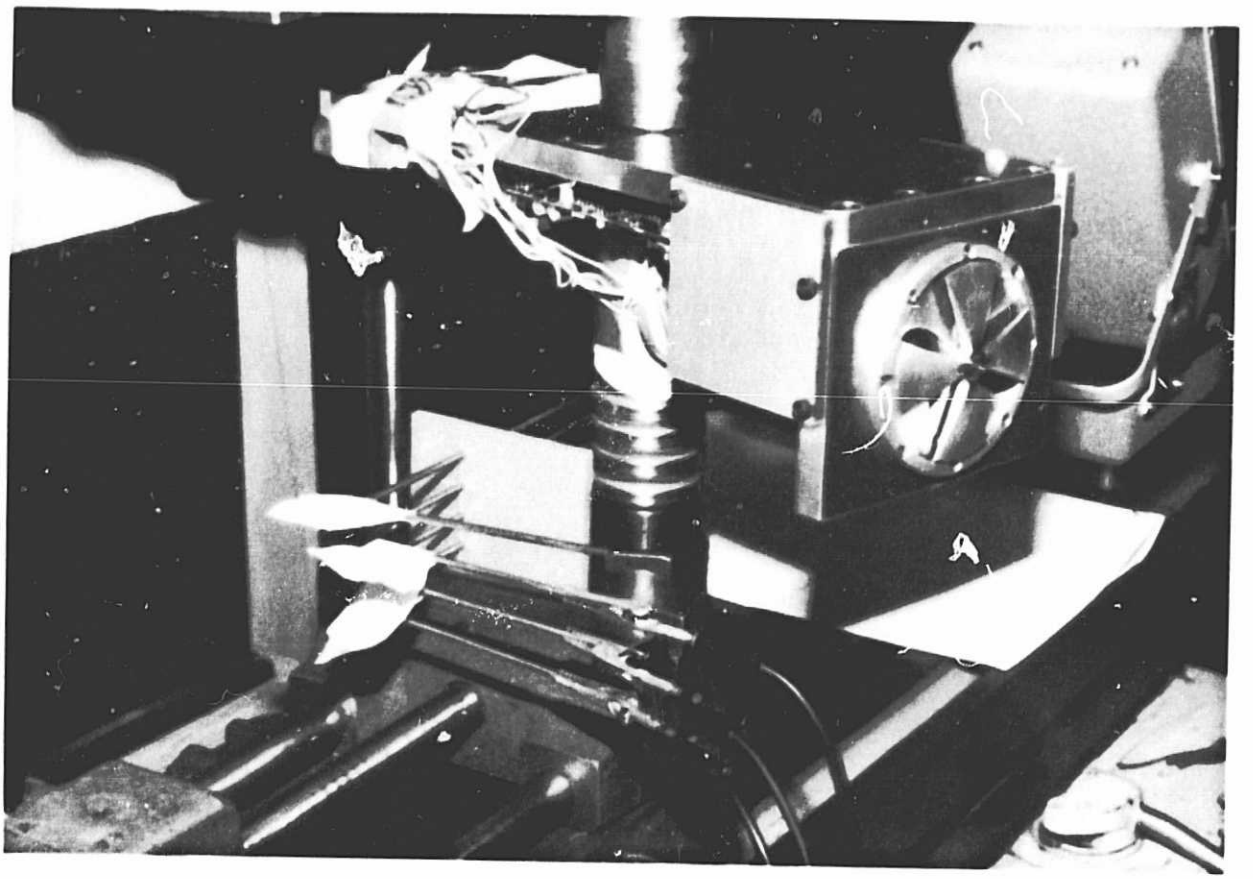

Figure 5.6 Spin-test fixture.

Table 5.1 Motor current at various rocket spin rates.

Bearing type	Spin rate (rpm)	(Hz)	Motor current (mA)
Bronze bushing	395	6.58	900
	500	8.33	1400
	680	11.33	current limited
Ball bearing	395	6.58	300
	500	8.33	350
	680	11.3	525

6. POST-FLIGHT SIGNAL PROCESSING

Flight data is to be provided by NASA in a digitized form on 1/2 inch computer tape. This data will be read by processing programs and analyzed to determine the results of the flight. Specific processing steps for analysis of the field meter output data are covered in this chapter. Listings of the major routines used to perform these functions are included in Appendix III.

6.1 Dynamic Range Restoration

The low gain field meter channel signal is compressed as described in Section 3.4. The compression function is characterized before flight as described in Section 5.6. The first step in post-flight processing is to remove the telemetry channel DC offset and restore the signal to the original range before compression. Since the high gain field meter channel is not compressed, restoration is omitted when that analysis is done.

A piecewise continuous model of the data restoration function is constructed from the compression characterization data. Each segment of the model is linear and can be represented by a linear equation. Finer compression characterization results in smaller linear segments of the restoration function model, resulting in less noise added to the signal during restoration. Ideally the compression characterization should be done in steps that are as small as the least significant bit of the digitized data words. If this is the case, linear segments of the restoration function are not needed. Restoration can then be done by a direct table lookup.

The linear segment of the restoration function associated with a given compressed sample is found from the magnitude and polarity of the sample.

The restored sample is obtained by evaluating the linear equation at the compressed sample point. In this fashion each sample of the data is restored to its precompression value. This is illustrated for one sample in Figure 6.1.

6.2 Digital Filtering

The electric field meter output contains some undesired frequency components, as shown by Figure 6.2. Only the rocket-spin modulated components of the 100 Hz chopping frequency are desired. Most of the unwanted signal can be filtered out with a band-pass filter centered at 100 Hz. Desirable characteristics of this filter are linear phase (to preserve the conduction and displacement signal components), about 20 Hz bandwidth (to pass both sidebands of the modulated chopping frequency), and greater than 60 dB attenuation outside of the 50 to 150 Hz band (to sufficiently reject the unwanted components). It is also desirable to have a flexible design procedure so that the filter can be easily matched to the data in case of unexpected output signals, or motor-speed or rocket-spin-rate variations. A finite impulse response (FIR) filter of length 65 easily meets these requirements. See Appendix I for a procedure to design this filter.

The frequency response of a filter that meets these requirements is shown in Figure 6.3.

The same data used to obtain Figure 6.2 was filtered by the filter of Figure 6.3. The resulting spectrum is shown in Figure 6.4.

The digital filter has a time delay associated with the linear phase characteristic. For an FIR filter the delay is a number of samples equal to 1/2 of the filter length minus 1 (Taylor [1983]), or 32 samples in this case. This delay must be taken into acount when the conduction and

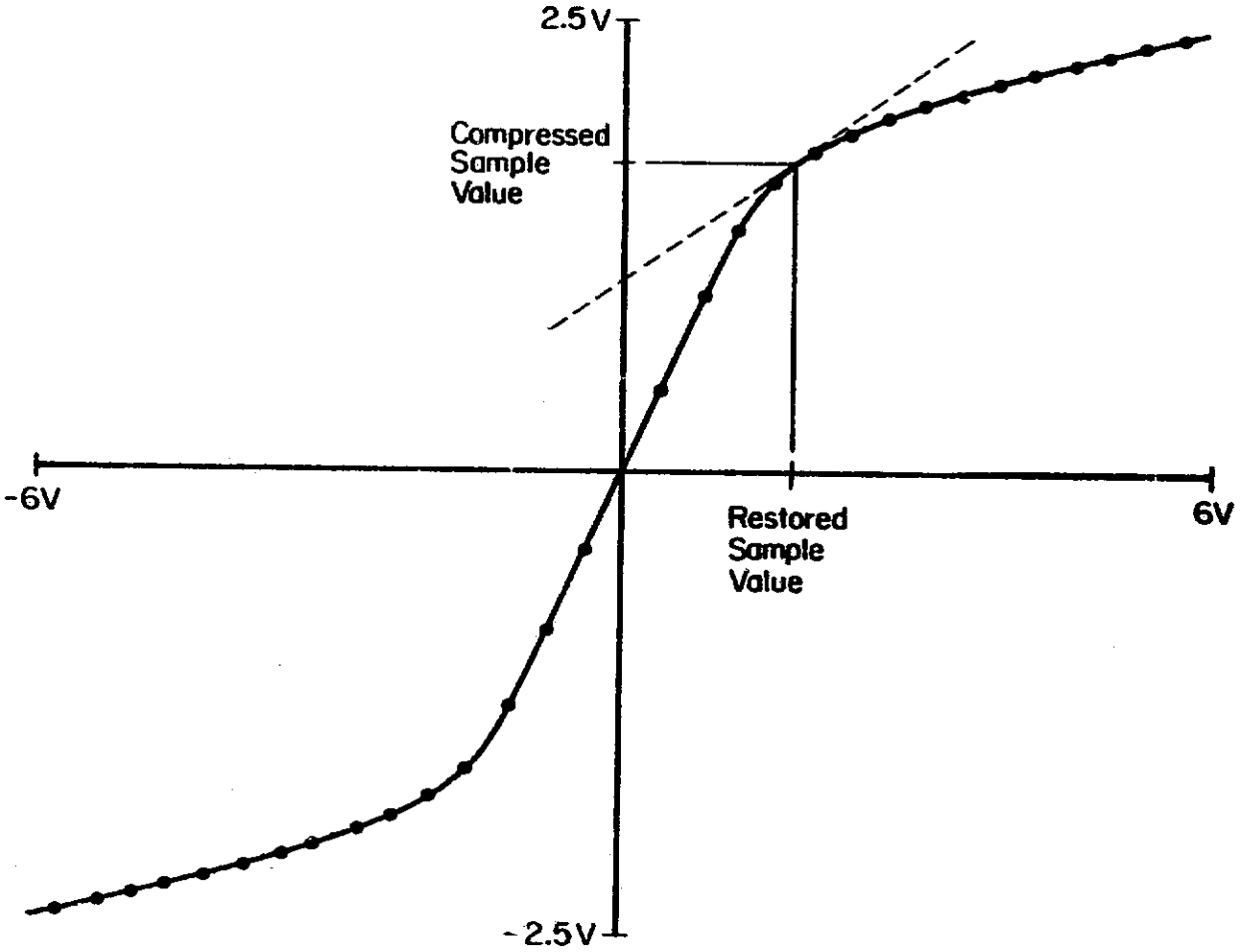

Figure 6.1 Compressed data restoration using piece-wise linear approximation.

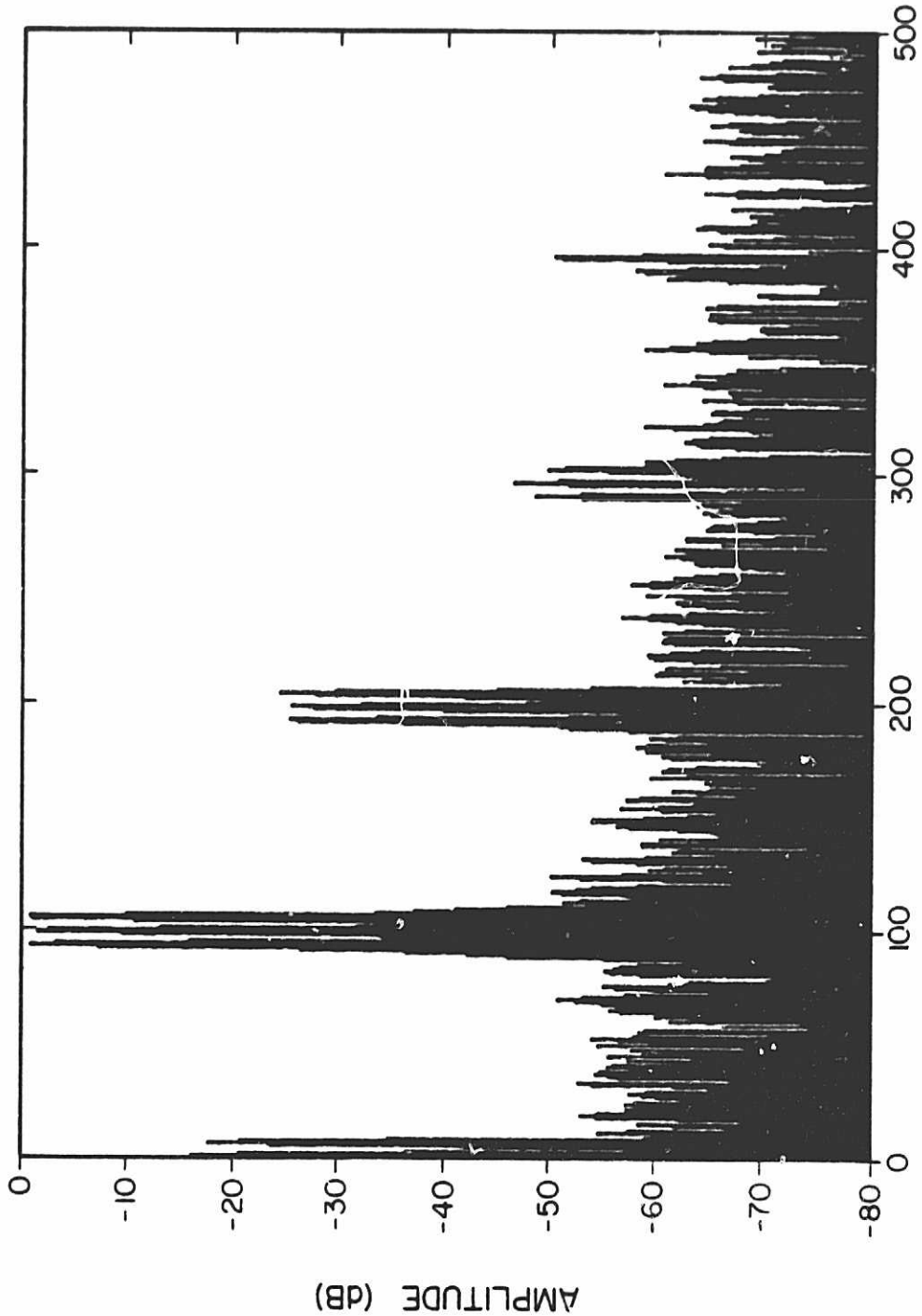

Figure 6.2 Spectrum of the output of the electric field meter with a peak applied electric field of 50 V/m at 6 Hz.

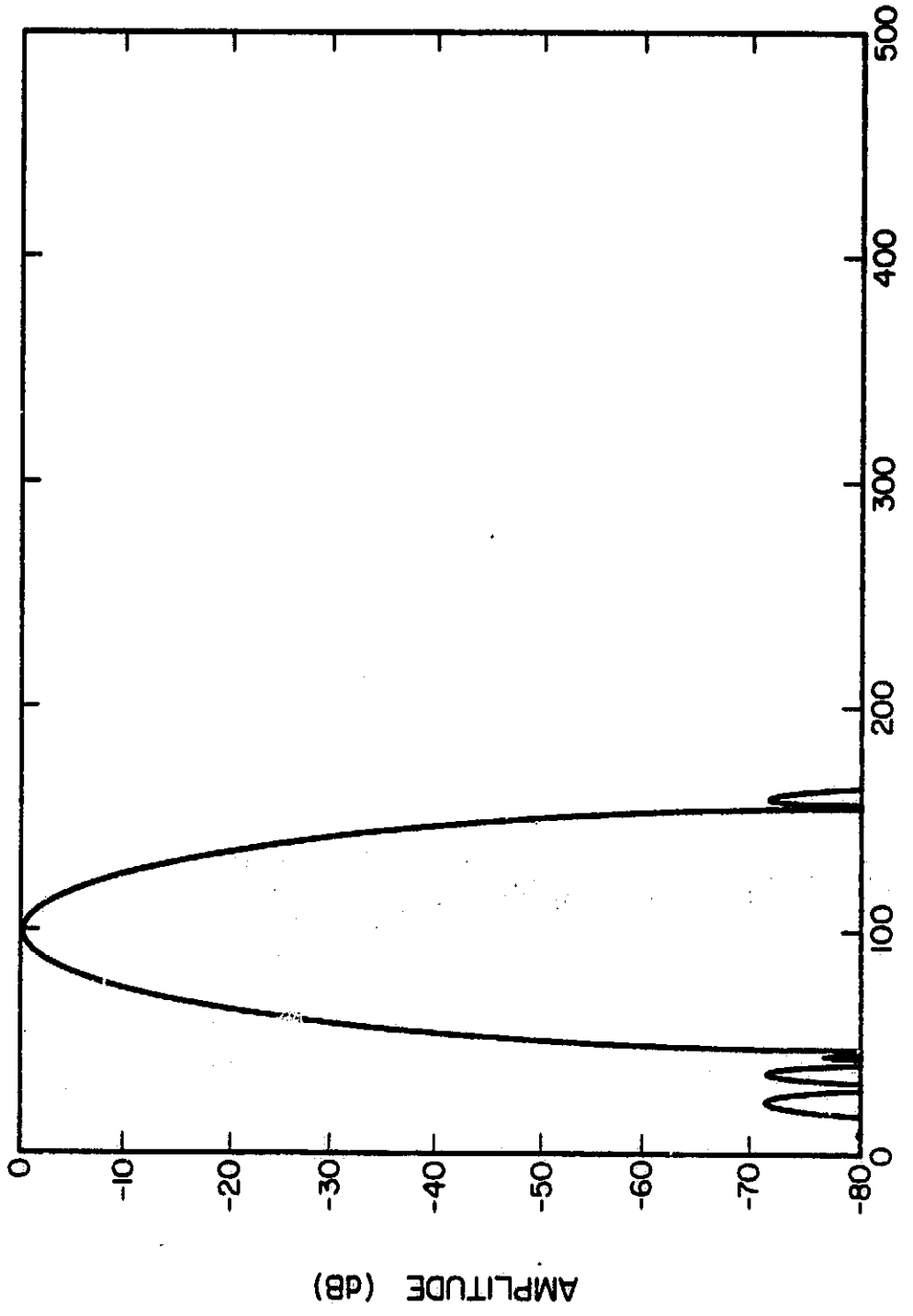

Figure 6.3 Digital filter frequency response.

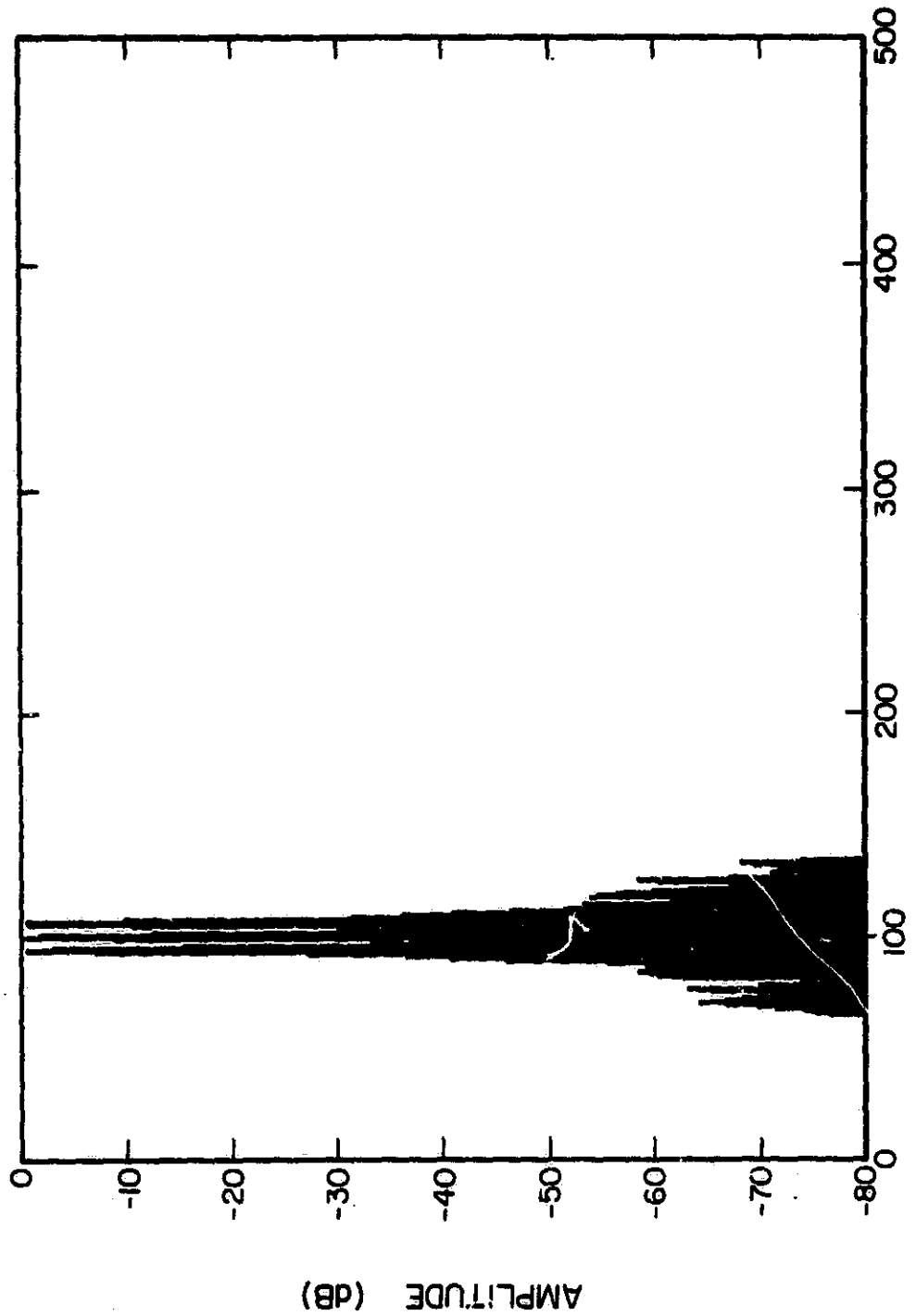

Figure 6.4 Spectrum of the filtered output of the electric field meter.

electric field signal components are separated.

6.3 Modulation Detection

After filtering, the 100 Hz component of the unwanted signal is still present. Its magnitude is several hundred mV. It would require a very long digital filter to notch out this signal (though that may still be a feasible method). A simpler approach is to detect the rocket-spin modulated 6 Hz sidebands.

If there were no unwanted 100 Hz signal present, the field meter output would look like the computer generated waveform of Figure 6.5a. This is the time-domain waveform of double-side-band suppressed carrier (DSB/SC) modulation. Demodulation can be accomplished by peak detecting the signal to obtain the envelope as in Figure 6.5b. The number of peaks can be doubled to increase the effective sampling rate of the envelope by first taking the absolute value of the DSB/SC waveform as in Figure 6.5c. This increases the probability of obtaining a peak closer to the actual envelope peak (the 100 Hz carrier and the 6 Hz modulation are not synchronized). The envelope magnitude is the sum of the two peak detected magnitudes in this case.

With the 100 Hz unwanted signal present, the waveform is more like a standard amplitude modulation (AM) waveform, since the unwanted signal is not modulated. The actual field meter digital band pass filtered output for a 10 V/m electric field is shown in Figure 6.6a. The same demodulation technique can be used to obtain the envelope. The magnitude of the 6 Hz modulation is just the difference between the maximum and minimum values of the detected envelope.

For a large amplitude electric field the output becomes more like the DSB/SC waveform as shown in Figure 6.6b for a 200 V/m electric field. The

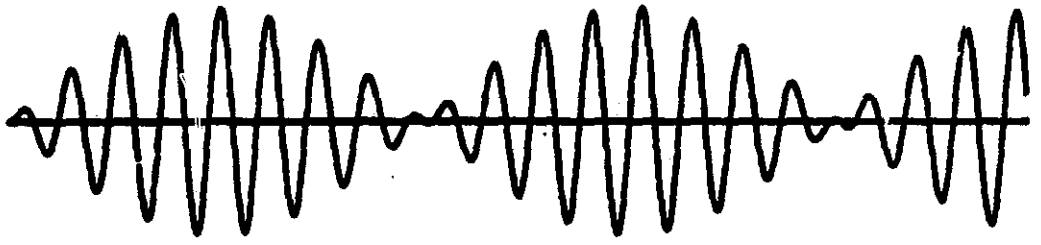

(a)

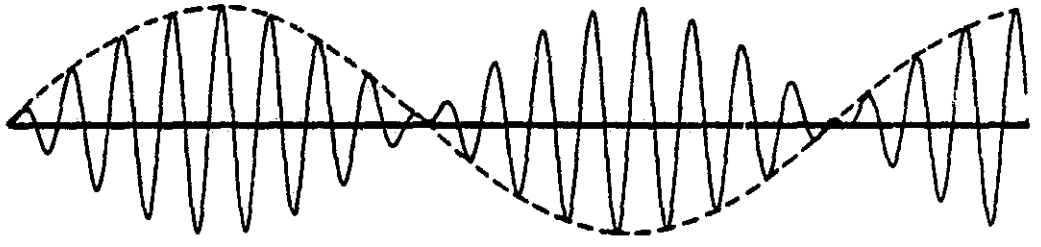

(b)

(c)

Figure 6.5 Detection of a DSB/SC signal. (a) waveform. (b) envelope. (c) detected envelope after absolute value.

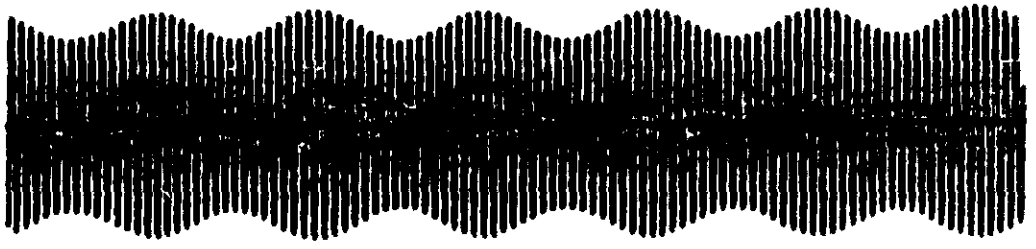

(a)

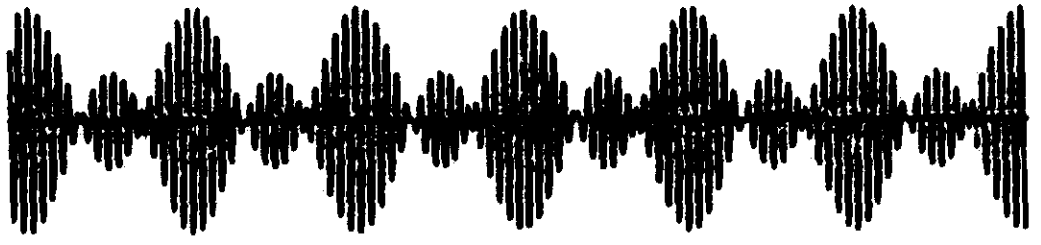

(b)

(c)

Figure 6.6 Effect of unwanted signal on envelope detection. (a) waveform for small fields. (b) waveform for large fields. (c) peak-detected envelope for large fields.

same demodulation technique can again be used but care must be taken in obtaining the peak envelope magnitude. The peak detected envelope of actual field meter data is shown in Figure 6.6c. The envelope magnitude is sum of the two local peak values, rather than the difference, as in the case when no 100 Hz unwanted signal is present.

This demodulation technique for obtaining the 6 Hz sideband magnitudes has some drawbacks. One is that the beating of the sampling frequency and the 100 Hz chopping frequency occurs if the sampling frequency is not an exact harmonic of the rotor frequency. This generates an apparent modulation that also gets detected. This is illustrated by computer generated data for a 100.5 Hz sinusoid and a 1 kHz sampling rate in Figures 6.7a and 6.7b. Another problem is that the carrier peak may not correspond to an electric field peak, resulting in a measurement that is lower than the actual magnitude.

6.4 Mechanical Noise

When attempting to measure small electric fields other unwanted signals becomes apparent. These are low-amplitude side bands of the 100 Hz carrier at 75 and 125 Hz. They correspond to the motor frequency (25 Hz) and so the source is assumed to be microphonic pickup from the motor and bearings. Another source was found to be vibration of spacing washers used to set the minimum rotor-sensor gap. This source was eliminated as described in Section 4.1.

This signal, together with the apparent beat modulation discussed in Section 6.3, is shown in Figure 6.8a after demodulation. One cycle of this signal corresponds to 8 samples of peak detected data so it can be effectively nulled out by replacing each sample with the average of the 8 samples around it. The result is shown in Figure 6.8b.

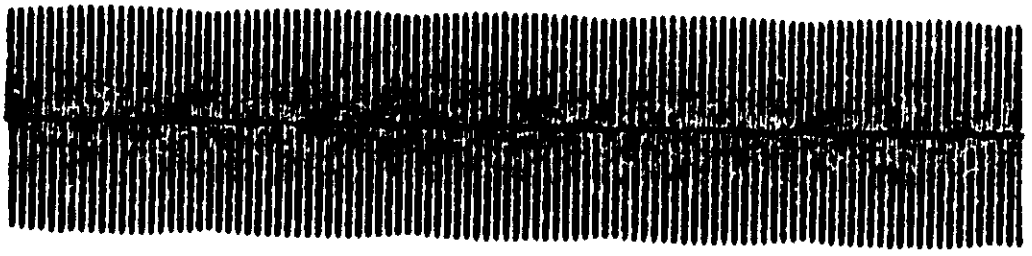

(a)

(b)

Figure 6.7 Effect of beating between the sampling frequency and the rotor chopping frequency for a pure sinusoid. (a) sampled waveform showing apparent modulation. (b) detected beat modulation on an expanded scale.

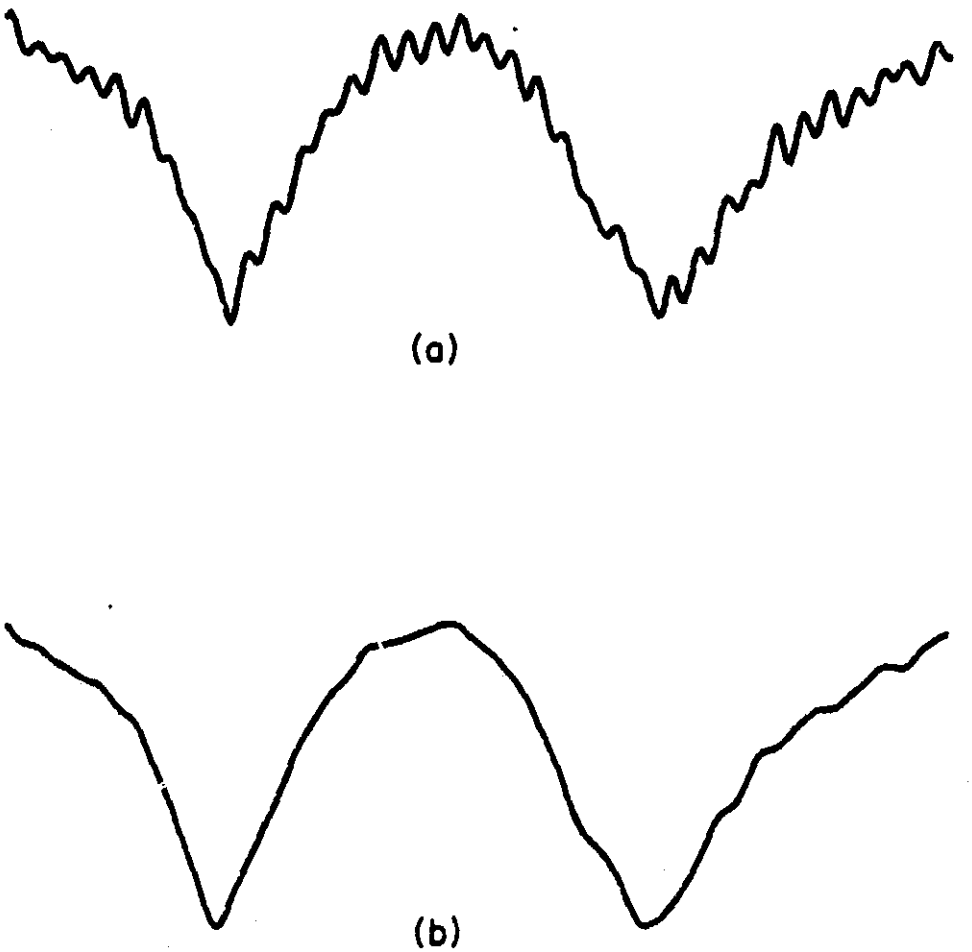

Figure 6.8 Elimination of an unwanted frequency component of the field meter output signal by averaging. (a) before averaging. (b) after averaging.

6.5 Signal Processing Examples

An example of the processing of the electric-field meter high-gain channel output for a small value of external electric field is shown in Figure 6.9. Figure 6.9a shows the output after the telemetry DC component is removed. Figure 6.9b shows the detected envelope without digital filtering. The amplitude scale is expanded. Figure 6.9c shows the output with digital band-pass filtering. Figure 6.9d shows the detected envelope of the filtered output.

An example of the low gain channel output for a large value of electric field is shown in Figure 6.10. Figure 6.10a shows the compressed output after the DC component is removed. The restored output is shown in Figure 6.10b. The envelope without digital filtering is shown in Figure 6.10c. The output and envelope with digital filtering are shown in Figures 6.10d and 6.10e.

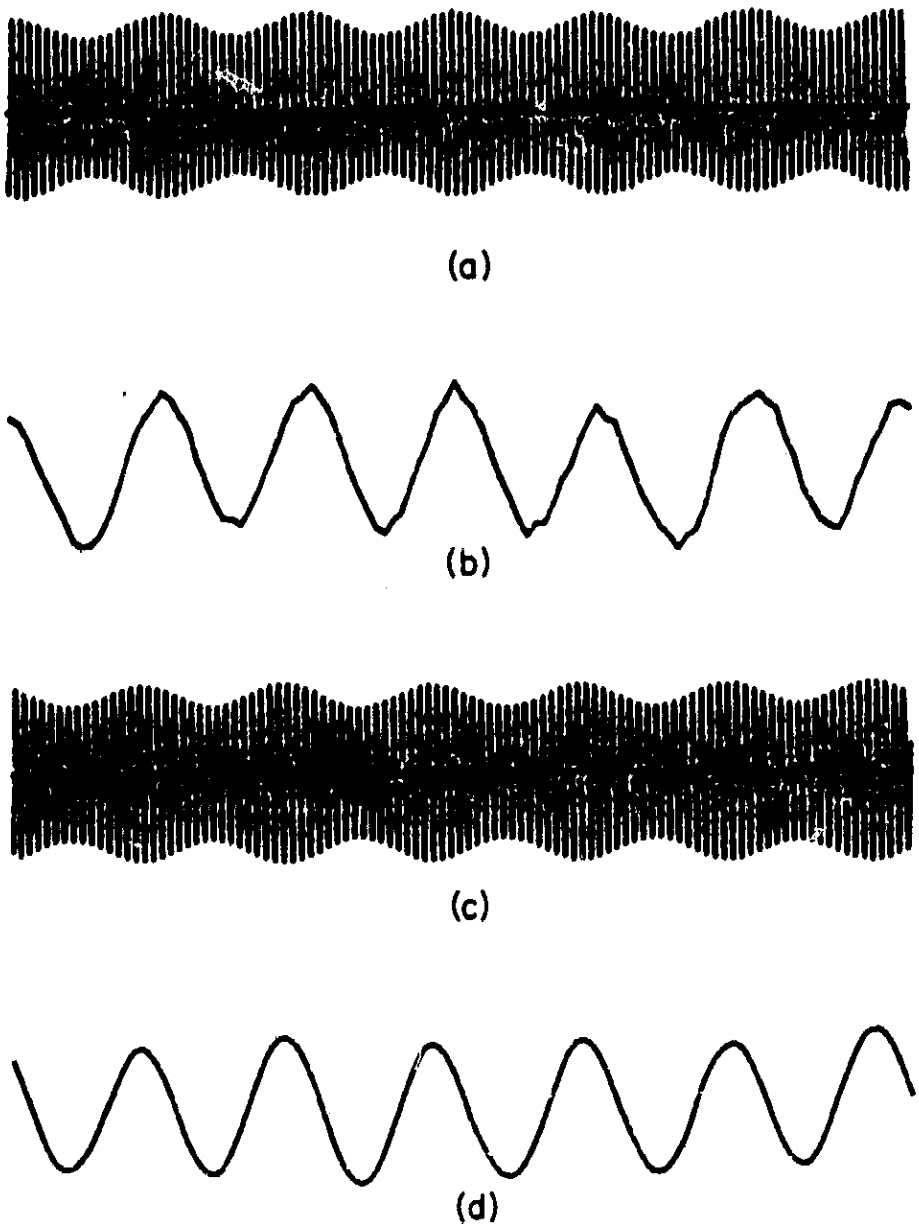

Figure 6.9 Processing of electric field meter high gain channel output for a small electric field. (See text for explanation.)

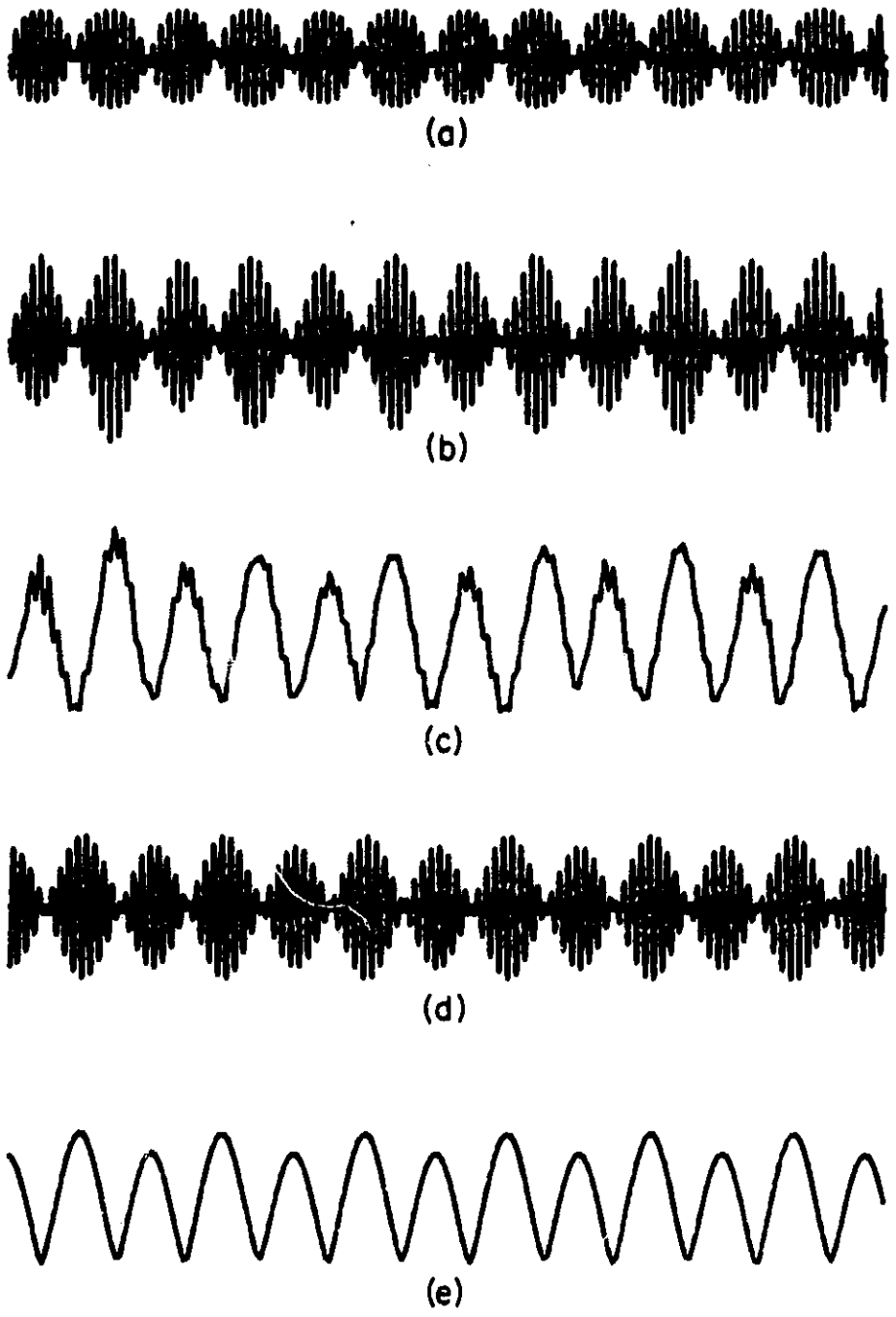

Figure 6.10 Processing of electric field meter low gain channel output for a large electric field. (See text for explanation.)

7. CONCLUSIONS AND SUGGESTIONS FOR FUTURE WORK

The electric field meter and the data processing algorithms have progressed to the point that a flight test is needed to evaluate the performance. The ability to measure electric fields in the desired range is shown by the actual field meter high-gain channel output waveform envelopes in Figure 7.1, and by the low-gain channel output waveform envelopes in Figure 7.2. There are, however, further improvements that can be made.

7.1 Electrical Systems

The electronics are satisfactory. The noise level and dynamic range are adequate to measure electric fields less than 1 V/m with no problems. If any changes are made in the electronics, they will probably come as a result of better understanding of the sensor unwanted signals or changes in desired experimental data, based on the results of the flight test.

7.2 Mechanical Systems

Mechanically the field meter is sound and should have no problems surviving the environment of a rocket launch. The new rotor shaft bearing configuration provides very good support and allows the motor bearing load to be reduced to a minimum. Electronic circuits will be encapsulated (in foam) before flight to prevent vibration breakage of connections and component mounts. This method has proved reliable in the past.

7.3 Electromechanical Systems

The rotor and sensor are the heart of the instrument. They have demonstrated the expected signals and some unexpected and unwanted ones. These unwanted signals are an obstacle to obtaining reliable measurements of low magnitude electric fields. The source of these signals is also not

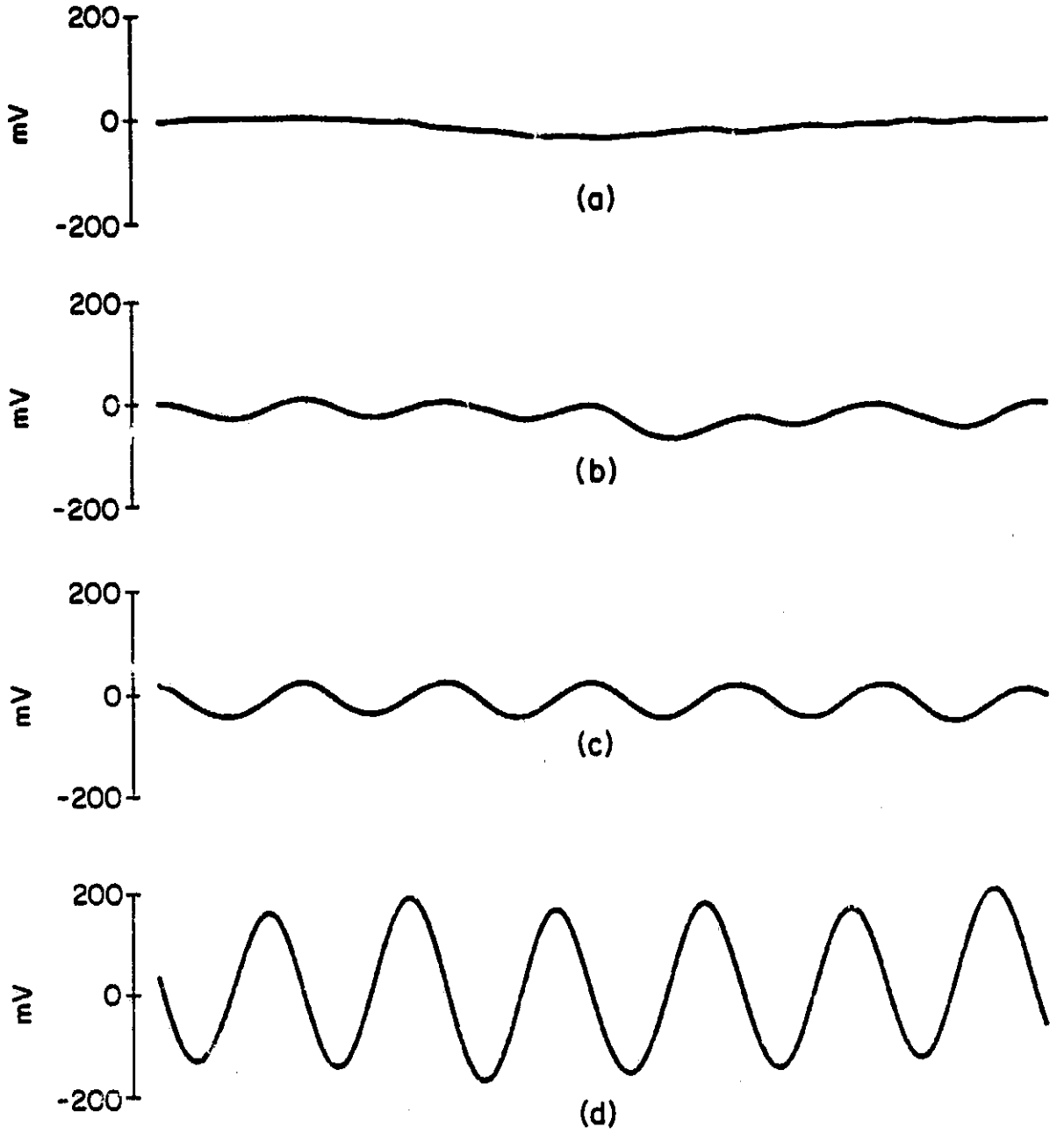

Figure 7.1 Outputs of the high gain channel of the electric field meter: (a) 0 V/m. (b) 1/2 V/m. (c) 1 V/m. (d) 5 V/m. These are shown as the detected envelopes of a 6 Hz modulation.

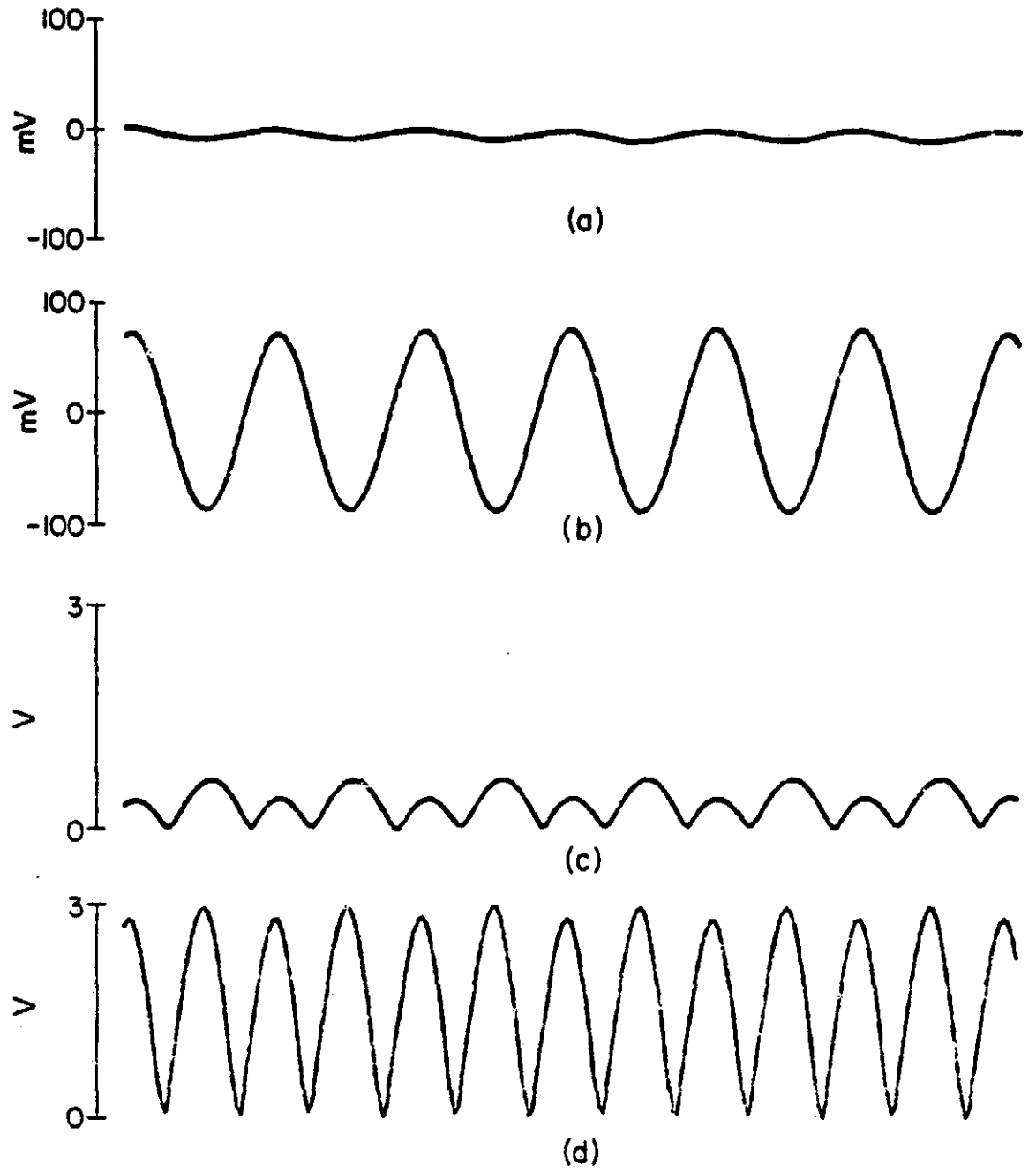

Figure 7.2 Outputs of the low gain channel of the electric field meter: (a) 1 V/m. (b) 20 V/m. (c) 100 V/m. (d) 500 V/m. These are shown as the detected envelopes of a 6 Hz modulation.

understood in detail. The action of the rotor covering and uncovering the sensor is known to be very important in the generation of these signals but the mechanism is unclear. A significant source of at least part of the signals is uneven work functions over surfaces in the rotor and sensor area. Treatment of the surfaces with colloidal graphite to create a uniform work function has produced improvement but does not account for all of the signals.

Another limiting factor is mechanical noise that is picked up by the electronics microphonically. The field meter currently has adequate mechanical performance, but this source of noise must be monitored to verify that the meter remains in good working order. Vibration testing to be performed at a later date may affect the mechanical performance.

7.4 Digital Filtering

Data processing schemes designed thus far are largly attempts to extract the desired electric field component of the signal from the unwanted signal. The band-pass digital filter minimizes the effect of the unwanted signal and noise outside of the passband. The current filter has good characteristics, but a filter with sharper transition regions would produce better results, especially if attenuation at the 75 and 125 Hz frequencies could be increased to reduce sensitivity to motor frequency related mechanical vibration.

The digital filter coefficients are generated in a very simple way (see Appendix I). There are some better ways that may result in filters with better frequency responses. If the the University of Illinois Cyber mainframe computer is used for data processing, a filter synthesis program using the McClellan-Parks algorithm is available. This program optimizes the filter according to user specified parameters and provides the best

filter possible for a given length. Another method that should work better than the method of Appendix I is called windowing. This consists of computing the infinite duration impulse response of the desired filter, truncating at the desired filter length and then windowing the result as described near the end of Appendix I. Chapter 5 of Oppenheim and Schafer [1975] explains this method.

If a much longer filter is used, it may be possible to have a notch at 100 Hz to stop the 100 Hz component of the unwanted signal. Digital filters could be cascaded to provide the various band pass and stop band characteristics desired. If 100 Hz can be removed from the signal, the modulation detection problem would match the case of the DSB/SC waveform described in Section 6.3. This would probably not be a tremendous advantage unless the 6 Hz modulation magnitude were to be determined using a spectral technique such as a fast fourier transform (FFT). In this case removal of any unwanted signal will help because of the windowing effect of the finite length FFT "smearing" the frequency components throughout the entire spectrum. Unwanted components would affect the magnitude or even mask the presense of the desired components. See Chapter 6 of Elliot and Rao [1982] or Harris [1978] for a more detailed presentation of this phenomenon.

If a spectral technique is used, then the best results would be obtained with a band-selectable fourier transform (Taylor [1983]). This technique would allow a high resolution FFT centered about the 100 Hz region of interest. As a comparison to a standard FFT, a 1024-point FFT gives 0.975 Hz spectral resolution over a 0 to 500 Hz band. A 1024-point band-selectable FFT could give 0.039 Hz spectral resolution over a 90 to 110 Hz band.

7.5 Modulation Detection

The modulation detection scheme has some problems as described in Section 6.3. The apparent modulation due to the beat frequency of the 100 Hz rotor signal and the sampling rate can be of a magnitude larger than a small amplitude electric field modulation. The frequency of the beat is also not precisely controlled and could be close enough to 6 Hz to obscure the desired data. This apparent modulation could be reduced by a sampling rate interpolation algorithm. Rather than take the maximum sample value as the peak value, compute new samples to effectively increase the sampling rate. The rate could be increased an arbitrary amount until the apparent modulation is reduced to an inconsequential magnitude. Laboratory measurements in this report were made with the motor speed adjusted very accurately to minimize the beat effect. This accuracy probably could not be maintained over the duration of a rocket flight.

An alternate approach to this problem would be to synchronize the sampling rate to the 100 Hz chopping frequency. This could be done by using a phase locked loop to multiply the encoder output signal up to the desired frequency (1 kHz) and using this as a sampling rate clock. This method would also de-sensitize the digital processing from motor speed variations.

Another approach would be to develop a crystal controlled frequency locked motor control to very precisely maintain a constant and accurate motor speed.

A similar effect occurs again when the magnitude of the detected envelope is to be determined. The rotor spin, the rocket spin, and the external electric field variation are all independent. Nothing ensures that the sensor will be completely uncovered when the normal component of

the electric field is at its maximum, or that the rocket angular position will align the field meter normal to the external field when the total horizontal electric field is at its maximum either. The peaks of the sampled signal are effectively samples of the envelope. Therefore, the peaks of the envelope should be determined by a sampling rate interpolation algorithm also.

7.6 Rocket-Tip Mounted Field Meter

A problem still exists for the electric field meter to be mounted in the nose of the rocket. Current data processing schemes are based on the expectation that the signal components associated with the external electric field are modulated by the rocket spin, while the unwanted signal and any others generated by the rocket will not be modulated. A nose-mounted meter will not be sensing a modulated field, therefore, the electric field component of the meter output will be inseparable from the unwanted signal.

There are some factors that work to make the nose field-meter measurement easier. The exposure factor at the tip of the rocket is expected to be at least 10. Also, laboratory tests showed a 70% reduction in unwanted signal magnitude with only a 20% reduction in the measured field value when the rotor-sensor gap was increased to 2.5 mm. A 1 V/m electric field results in a 36 mV peak output signal from the high gain channel. If the unwanted signal magnitude can be maintained at its minimum (about 0.5 V peak at the high gain channel output), then an optimistic unwanted signal value of 150 mV peak will correspond to an external electric field magnitude of 0.5 V/m, for an exposure factor of 10 and a rotor gap of 2.5 mm. This would make a 1 V/m external field barely measurable with the tip mounted field meter.

The tip-mounted field meter must also have some minor mechanical modifications. During launch it will be subject to high acceleration forces so the rotor shaft must have axial support in the opposite direction as the shaft in the horizontally mounted meter. After burn out there will be no centrifugal force to hold the shaft coupling against the rear ball bearing to maintain the rotor-sensor spacing. The front deck bronze bushing should be replaced by the same type ball bearing used in the preamplifier chamber wall. They have the same dimensions and so are interchangeable. The rotor-sensor gap must now be obtained with spacers between the rotor and the front deck ball bearing. These will not vibrate to produce mechanical noise because they will rotate with the shaft and bearing inner race. After burn the rotor must be held against the spacers by a spring mounted between the preamplifier chamber wall bearing and the coupling spline. Refer to Figure 7.3 for a diagram of this configuration.

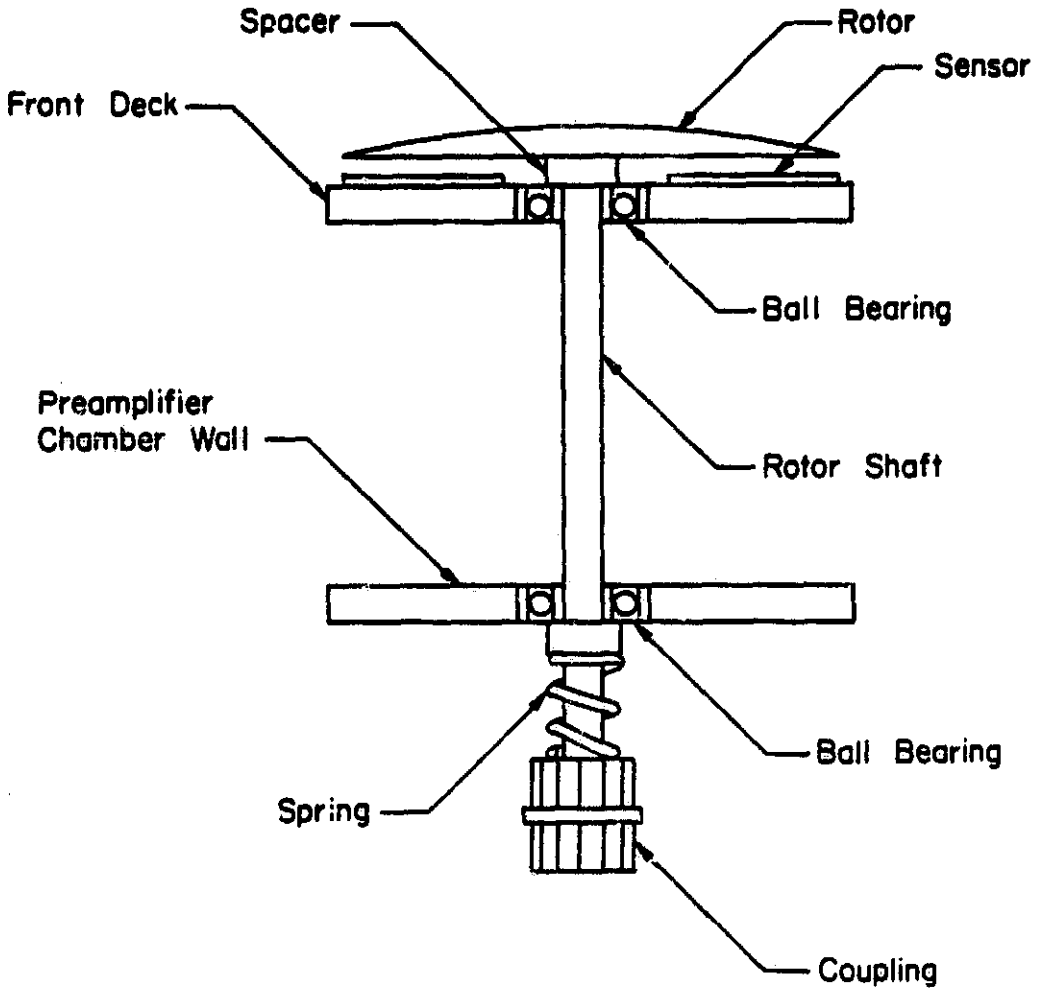

Figure 7.3 Configuration of the rotor for the tip-mounted field meter.

APPENDIX I. DIGITAL FILTER DESIGN

The structure of an finite impulse response (FIR) filter is depicted in Figure I.1. It is readily seen from this diagram that the impulse response of the filter is just the coefficients on the taps of the delay register. Any type filter can be synthesized by determining its impulse response and using it for the filter coefficients.

A procedure for the design of an FIR filter will now be given with the filter described in Section 6.2 as an example. The method used is frequency sampling of the desired filter response and windowing the impulse response obtained from the frequency sampling. These techniques are described in Chapter 5 of Oppenheim and Schafer [1975]. Other techniques exist but this one is very simple conceptually and is easily implemented with existing fast fourier transform (FFT) algorithms.

In order to obtain a linear phase, real filter (a real input results in a real output, there are no complex coefficients) the desired response must be sampled as an even real function with respect to the frequency origin. An inverse fast fourier transform (IFFT) is done on the sampled desired frequency response to obtain the filter impulse response. For convenience a power-of-two FFT is used to perform the IFFT. See Chapter 10 of Brigham [1974] for more information on FFT algorithms.

The output of a power-of-two IFFT with an even real input is symmetrical about the $n = 0$ sample. The IFFT output must be circular shifted to put the $n = 0$ sample in the center of the filter. Since the output of a power-of-two IFFT is an even number of samples, this results in a filter that is symmetrical about its center with the exception of having an extra coefficient on one end. In order to be linear phase, an FIR filter must be symmetric about its center. The extra sample at one end of the

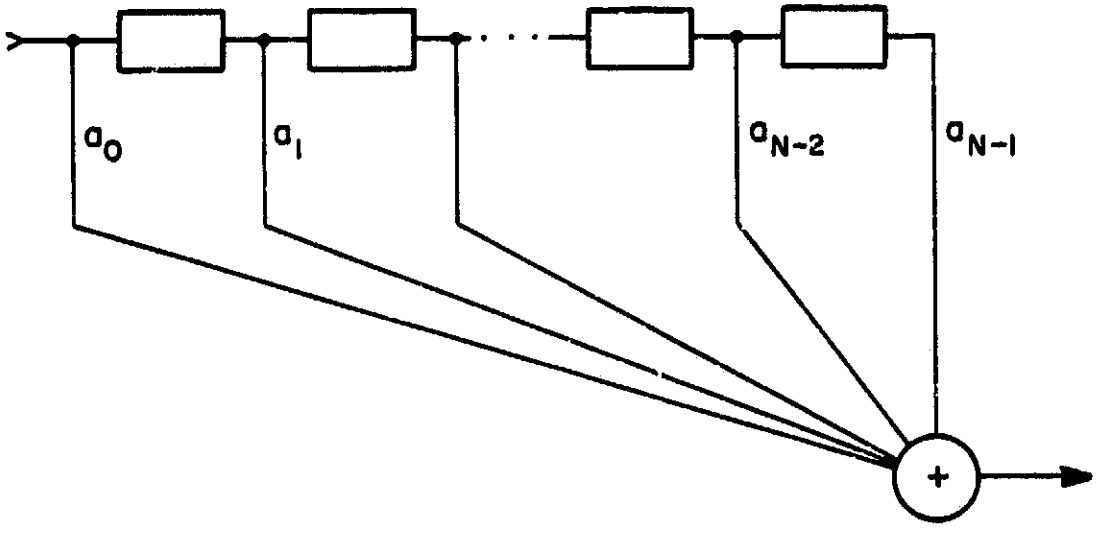

Figure I.1 FIR digital filter structure.

filter can be thrown away or another of the same value added at the other end to satisfy the requirement for linear phase. In either case the filter transfer function will be only minimally affected.

After obtaining a filter based on the impulse response of the sampled desired response, we can compute the actual frequency response by doing an FFT on the coefficients. The length of the FFT should be at least twice the filter length (preferably even longer) so that an accurate representation can be obtained. If the FFT length is too short, some of the output points may coincide with nulls in the filter response and the actual stop band magnitude of the filter will not be seen.

At this point the filter stop-band attenuation is unacceptable. To increase the stop-band attenuation a windowing technique is used. The filter coefficients are multiplied with a window having low-amplitude sidelobes resulting in lower filter sidelobe amplitude at the expense of increasing the filter passband width. Refer to Chapter 6 of Elliot and Rao [1982] or Harris [1978] for more information on window theory and application.

For this application a length 64 IFFT is used. The sampled desired frequency response as input to the IFFT is shown in Figure I.2. The samples are of different magnitudes to center the passband at 100 Hz. This is required because 100 Hz does not fall on an integer value of the IFFT input. A length 65 filter is obtained by adding an extra sample. The impulse and frequency responses (computed with a length 1024 FFT) before windowing are shown in Figure I.3 and Figure I.4. A Blackman window (Oppenheim and Schafer [1975]), defined by the function

$$w(n) = 0.42 - 0.5\cos(2\pi n/(N-1)) + 0.08\cos(4\pi n/(N-1)) \qquad (I.1)$$

where $0 \leq n \leq N - 1$, n denotes the filter coefficient and N is the filter

Figure I.2 Band-pass filter sampled desired frequency response as input to a length 64 IFFT.

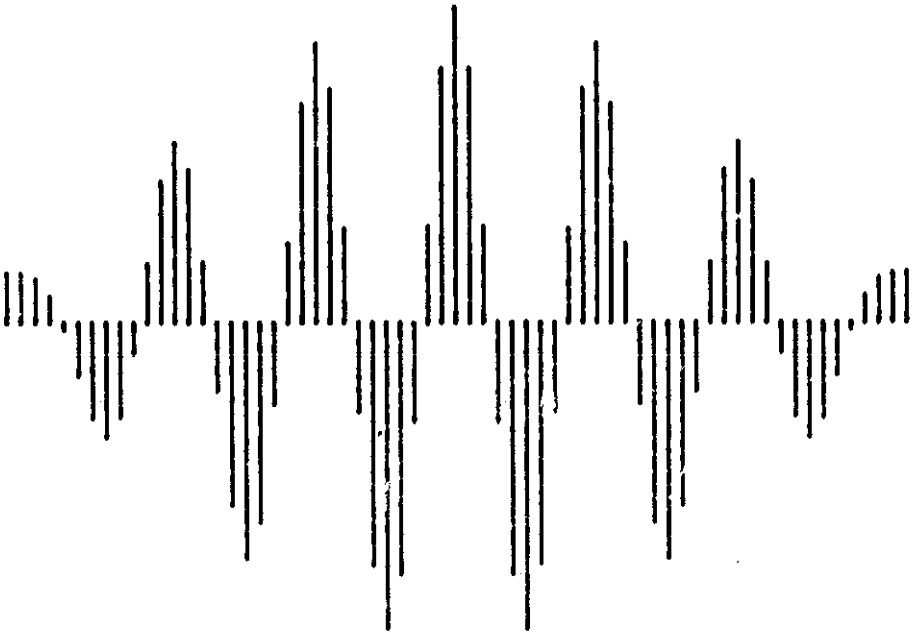

Figure I.3 Band-pass digital filter impulse response before windowing.

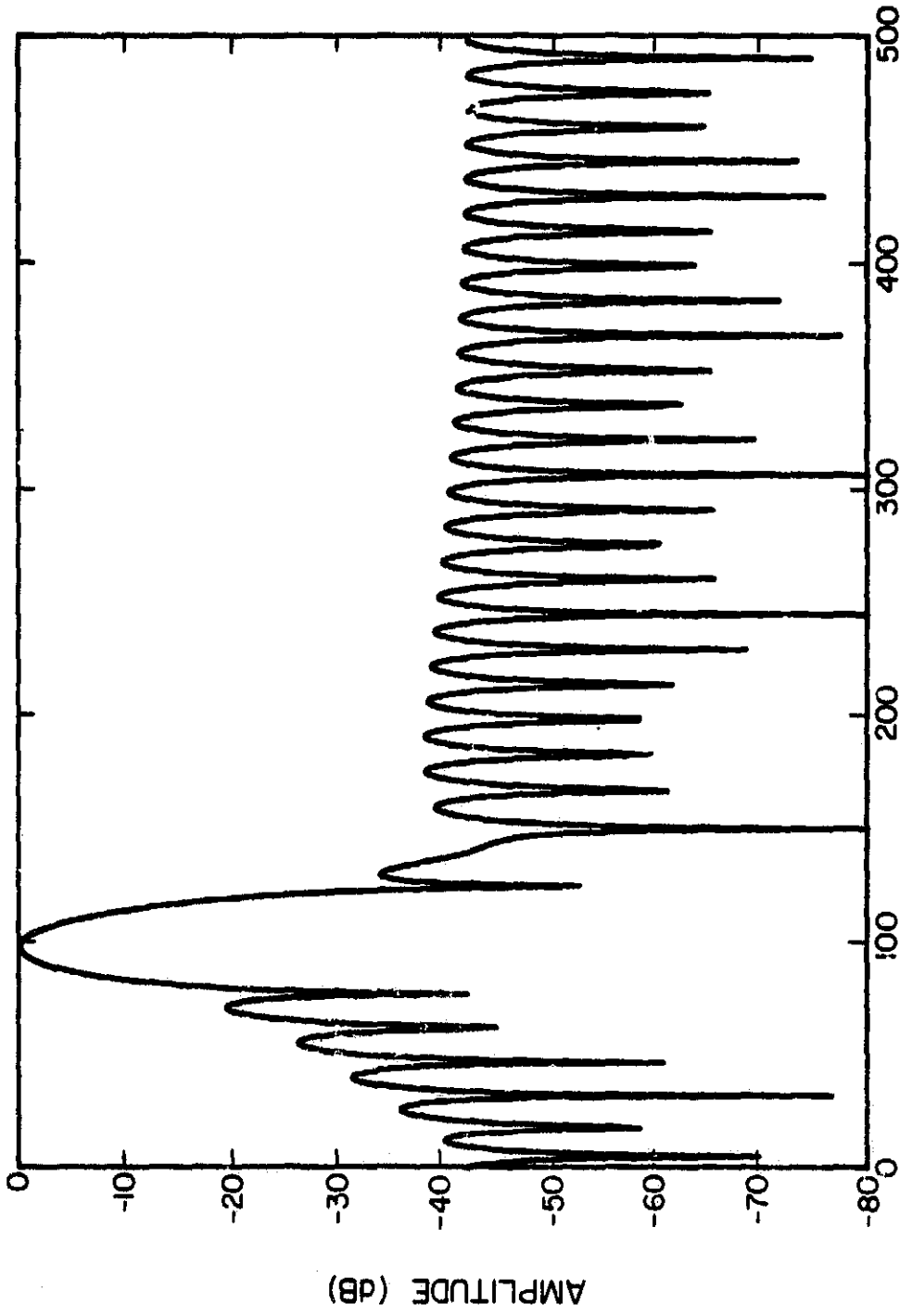

Figure I.4 Band-pass digital filter frequency response before windowing.

length, is multiplied with the filter coefficients. This window is shown in Figure I.5. The resulting impulse response is shown in Figure I.6. The frequency response is shown in Figure 6.3. The coefficients for this filter are listed in Table I.1.

C - 2

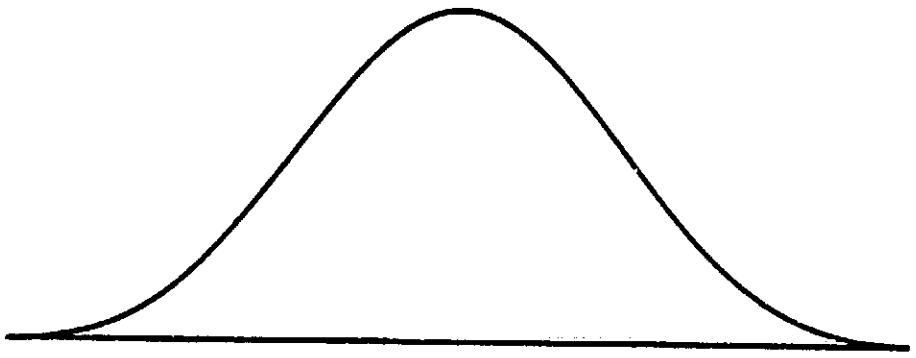

Figure I.5 Blackman window.

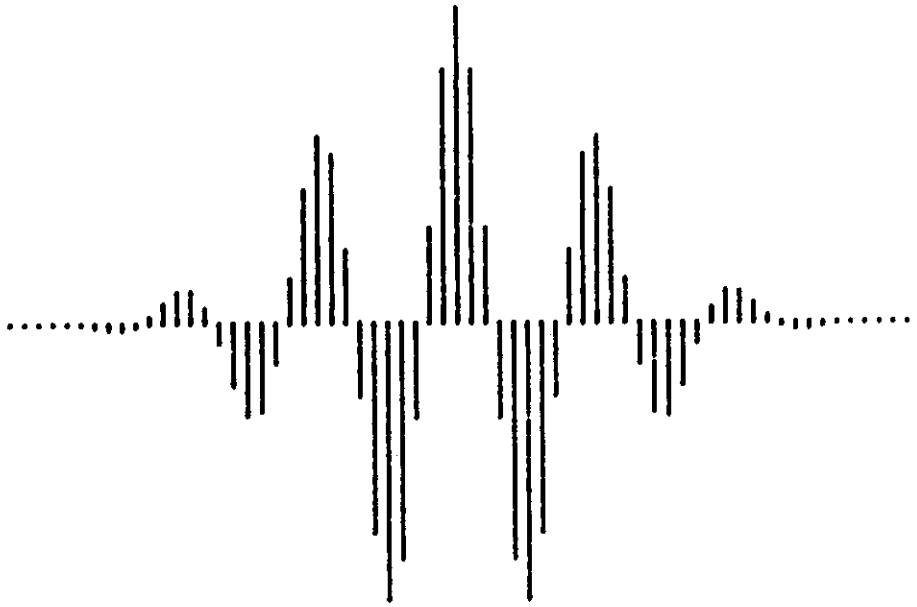

Figure I.6 Band-pass digital filter impulse response after windowing.

Table I.1 Digital filter coefficient listing.

n	a_n	n	a_n
0	5.88529225E-019	33	7.10098661E-002
1	1.21193136E-005	34	2.64276140E-002
2	4.35164442E-005	35	-2.6526675E-002
3	6.03161191E-005	36	-6.6180481E-002
4	-2.8553542E-005	37	-7.7654490E-002
5	-3.4638465E-004	38	-5.8875294E-002
6	-9.3222776E-004	39	-2.0414666E-002
7	-1.5764790E-003	40	2.02969668E-002
8	-1.7434669E-003	41	4.71900754E-002
9	-7.3761250E-004	42	5.21698609E-002
10	1.84017763E-003	43	3.73047392E-002
11	5.52246454E-003	44	1.22238936E-002
12	8.67926125E-003	45	-1.1332963E-002
13	8.90080246E-003	46	-2.4845255E-002
14	4.17160834E-003	47	-2.5833597E-002
15	-5.5775159E-003	48	-1.7422620E-002
16	-1.7422620E-002	49	-5.5775159E-003
17	-2.5833597E-002	50	4.17160834E-003
18	-2.4845255E-002	51	8.90080246E-003
19	-1.1332963E-002	52	8.67926125E-003
20	1.22238936E-002	53	5.52246454E-003
21	3.73047392E-002	54	1.84017763E-003
22	5.21698609E-002	55	-7.3761250E-004
23	4.71900754E-002	56	-1.7434668E-003
24	2.02969668E-002	57	-1.5764790E-003
25	-2.0414666E-002	58	-9.3222776E-004
26	-5.8875294E-002	59	-3.4638465E-004
27	-7.7654490E-002	60	-2.8553542E-005
28	-6.6180481E-002	61	6.03161191E-005
29	-2.6526675E-002	62	4.35164442E-005
30	2.64276140E-002	63	1.21193136E-005
31	7.10098661E-002	64	5.88529225E-019
32	8.83500000E-002		

APPENDIX II. FIR DIGITAL FILTER ENBW

The noise bandwidth of a noiseless analog filter is defined to be the bandwidth of an ideal rectangular filter that has the same output rms voltage as the analog filter when the inputs are white broad-band noise processes (Gray and Meyer [1977]). This same concept can be applied to a digital filter. This discussion is geared to apply to a FIR filter that is implemented with the structure of Figure I.1.

If the input noise spectrum is assumed flat within the filter passband, then the noise output of the filter will be shaped to match the filter frequency response. To calculate the FIR filter equivalent noise bandwidth (ENBW), first obtain the frequency response by performing an FFT on the filter coefficients. The FFT output contains the frequency response for both positive and negative frequencies from DC to one half of the sampling rate so only one half of the output is needed. The magnitude of the output samples represents the filter transfer function magnitude at corresponding frequencies. The largest sample magnitude is the maximum gain of the filter. Square each sample magnitude and add them together to get the output mean square voltage. Divide this value by the square of the maximum filter gain. Since the FFT output points are probably not spaced at 1 Hz intervals, a final adjustment must be made. Multiply by the frequency step per FFT output sample (or the sampling rate divided by the FFT length). This gives the final result for the ENBW in Hz. The formula is:

$$ENBW = F \left[\frac{\sum_{i=o}^{N/2} |n_i|^2}{|\max n_i|^2} \right] \qquad \text{(II.1)}$$

where F is the frequency per sample.

The ENBW for the filter with response shown in Figure 6.3 is 30 Hz. This is the bandwidth used in the Section 3.2 preamplifier noise calculations.

APPENDIX III. DIGITAL SIGNAL PROCESSING ROUTINES

The routines listed here are simplified versions of those used to perform digital filter synthesis, digital filtering, demodulation and do FFT spectral analysis. They are written in Version 2.1 Pascal for Hewlett Packard Series 200 computers.

```
{ Digital Signal Processing routines
  for electric field meter data processing
  University of Illinois
  Urbana-Champaign
  Aeronomy laboratory
  David Burton   6 Jun 1984 }

{ These are the global constants and variables }

CONST
   maxM = 10;              { 2^10=1024 }
   maxN = 1024;            { Max FFT length }
   maxH = 513;             { Max filter length }
   Len  = maxN+maxH+1; { # of analog smpls }
   PI   = 3.14159265358979323846;

TYPE
   Data = ARRAY[1..Len] of REAL;
   Dataptr = ^Data;
```

```
VAR
   Fs:  REAL;        { Sampling rate }
   M,N: INTEGER;     { N is FFT length, M=2^N }
   Choice: CHAR;     { Input var for user choices }
   INR: ARRAY[1..maxN] of REAL;
   X  : ARRAY[1..maxN] of REAL;
   Y  : ARRAY[1..maxN] of REAL;
        { INR is an FFT input array.  Before the
          FFT is executed INR should be copied
          into X and Y set to 0.  After the FFT
          INR will be undisturbed, X will have
          the real FFT output and Y will have the
          imaginary FFT output. }
   H  : ARRAY[0..maxH-1] of REAL;
        { Digital filter coef's }
   Peak: ARRAY[1..310] of REAL;
        { Waveform envelope obtained by peak
          detecting }
   Inp: ^Data; { Digitized waveform }
   Out: ^Data; { Filtered waveform }
   Filter_length :INTEGER;
   Out_stop :INTEGER;
        { Last valid data point in the Out array.
          When Inp is filtered it takes one
          filter length of data to get the filter
          working.  Therefore Out has fewer valid
          data points than Inp. }


PROCEDURE BLACKMAN_WINDOW;
   { This procedure performs the Blackman window-
     ing of the digital filter impulse response.
     The impulse response should be in the array
     H when calling this procedure.  The windowed
     impulse response is in H after completion. }
   VAR  Wn,Q :REAL;
        I   :INTEGER;
   BEGIN
   FOR I:=0 TO (Filter_length-1) DO
     BEGIN
     Q:=(2*PI*I)/(Filter_length-1);
     Wn:=0.42-0.5*COS(Q)+0.08*COS(2*Q);
     H[I]:=H[I]*Wn;
     END;
   END;
```

```
PROCEDURE FFT;
  { This is a standard power of two FFT routine.
    It is adapted from the FFT ALGOL computer
    subroutine of Figure 10-8 from Brigham [1974].
    The data to be transformed should be in the X
    array and the Y array should be zeroed before
    calling FFT. }
  VAR  N2,M1,I,K,L,P          :INTEGER;
       Arg,C,S,Q,Treal,Timag  :REAL;

  FUNCTION ATOB(A,B:INTEGER):INTEGER;
     VAR I,Temp :INTEGER;
     BEGIN
     Temp:=1;
     FOR I:=1 TO B DO
        Temp:=A*Temp;
     ATOB:=Temp;
     END;

  FUNCTION BITREV(J,M:INTEGER):INTEGER;
     VAR I,J1,J2,K  :INTEGER;
     BEGIN
     J1:=J;
     K:=0;
     FOR I:=1 TO M DO
       BEGIN
       J2:=J1 DIV 2;
       K:=K*2+(J1-2*J2);
       J1:=J2;
       END;
     BITREV:=K;
     END;
```

```
BEGIN
Q:=2*PI/N;
N2:=N DIV 2;
M1:=M-1;
K:=1;
FOR L:=1 TO M DO
  BEGIN
  REPEAT
    BEGIN
    FOR I:=1 TO N2 DO
      BEGIN
      P:=BITREV((K-1) DIV ATOB(2,M1),M);
      Arg:=Q*P;
      C:=COS(Arg);
      S:=SIN(Arg);
      Treal:=X[K+N2]*C+Y[K+N2]*S;
      Timag:=Y[K+N2]*C-X[K+N2]*S;
      X[K+N2]:=X[K]-Treal;
      Y[K+N2]:=Y[K]-Timag;
      X[K]:=X[K]+Treal;
      Y[K]:=Y[K]+Timag;
      K:=K+1;
      END;
    K:=K+N2;
    END;
  UNTIL K-1>=N;
  K:=1;
  M1:=M1-1;
  N2:=N2 DIV 2;
  END;
  FOR K:=2 TO N+1 DO
    BEGIN
    I:=BITREV(K-1,M)+1;
    IF I>K THEN
      BEGIN
      Treal:=X[K];
      Timag:=Y[K];
      X[K]:=X[I];
      Y[K]:=Y[I];
      Y[I]:=Treal;
      Y[I]:=Timag;
      END;
    END;
END;
```

```
PROCEDURE IFFT;
   { Performs the inverse FFT on the data in the
    X and Y arrays.  Puts the real output in the
    X array into the INR array.  To perform the
    IFFT the data in the X and Y arrays are
    divided by the length N and the complex
    conjugate is taken by negating the imaginary
    input in the Y array and doing an FFT. }
   VAR I:INTEGER;
    BEGIN
    FOR I:=1 TO N DO
      BEGIN
      X[I]:=X[I]/N;    {pre-scale the input}
      Y[I]:=-Y[I]/N;   {and complex conjugate}
      END;
    FFT;
    FOR I:=1 TO N DO
      BEGIN
      INR[I] := X[I];
      END;
    END;



PROCEDURE GEN_COEF;
   { This procedure performs the circular shift
     on the IFFT output to generate the FIR
     digital filter coefficients. }
   VAR I,J :INTEGER;
       K   :REAL;
   BEGIN
   Filter_length:=N+1;
   FOR I:=(N DIV 2)+1 TO N DO
     BEGIN
     H[I-(N DIV 2)-1]:=X[I];
     H[I-1]:=X[I-(N DIV 2)];
     END;
   H[N]:=H[0];
   END;
```

```
PROCEDURE FILTER;
   { This procedure performs the filtering of
     the data in Inp with the filter coefficients
     in H and the result is placed in Out. }
   VAR I,J  :INTEGER;
       Out_copy: ^Data;
   BEGIN
   FOR I:=1 TO Len-Filter_length+1 DO
      BEGIN
      Out^[I]:=0;
      FOR J:=0 TO Filter_length-1 DO
         Out^[I]:=Out^[I]+
                  H[J]*Inp^[I+Filter_length-1-J];
      END;
   Out_stop:=Len-Filter_length+1;
   END;



PROCEDURE COMPUTE_RMS;
   { This procedure computes the RMS value of the
     data in the INR array. }
   VAR I    :INTEGER;
       Vrms :REAL;
   BEGIN
   Vrms:=0;
   FOR I:=1 TO N DO
      BEGIN
      Vrms := SQR(INR[I]) + Vrms;
      END;
   Vrms := SQRT(Vrms/N);
   WRITELN;
   WRITELN (' RMS value is  ',Vrms:12);
   END;
```

```
PROCEDURE COMPUTE_ENBW;
   { This procedure computes the equivalent noise
     bandwidth of the digital filter with
     coefficients in H according to the formula
     in appendix 2. }
   VAR  I:INTEGER;
        ENBW,Max_gain,S :REAL;
   BEGIN
   FOR I:=1 TO Filter_length DO
      BEGIN
      X[I] := H[I-1]; { Put H into FFT arrays }
      Y[I] := 0;
      END;
   FOR I:=Filter_length+1 TO N DO
      BEGIN
      X[I] := 0;       { Pad FFT arrays with 0 }
      Y[I] := 0;
      END;
   FFT;      { Do FFT to get freq. resp. }
   ENBW:=0;
   FOR I:=1 TO (N DIV 2)+1 DO
      BEGIN
      S:=SQR(X[I])+SQR(Y[I]);  { Sum of squares }
      ENBW:=ENBW+S;
      IF Max_gain<S THEN Max_gain:=S;
      END;
   WRITELN;
   ENBW:=ENBW/Max_gain;
   WRITELN('       ENBW = ',ENBW:10);
   ENBW:=(Fs/N)*ENBW;
   WRITELN('    or ENBW = ',ENBW:10,' Hz');
   WRITELN('     for Fs = ',Fs:10);
   END;
```

```
PROCEDURE PEAK_DET;     {peak detector}
  { This procedure peak detects the waveform in
    Out.  Absolute value is taken.  Peaks are
    found by looking for local maximums.  The
    user has the option of doing an 8 sample
    average on the peak detected data.  The
    output is in the Peak array. }
  VAR  I,J :INTEGER;
       S :ARRAY[1..3] of REAL;
       Ave,P  :REAL;
   BEGIN
   FOR I:=1 TO 310 DO
      BEGIN
      Peak[I] := 0;
      END;
   S[1]:=ABS(Out^[2]);
   S[2]:=ABS(Out^[1]);
   S[3]:=ABS(Out^[1]);
   Ave:=0;
   J:=1;
   For I:=1 TO Out_stop-2 DO
      BEGIN
      S[3]:=S[2];
      S[2]:=S[1];
      S[1]:=ABS(Out^[I+2]);
      IF (S[2]>S[1]) AND (S[2]>S[3]) AND (J<311) THEN
         BEGIN
         Peak[J]:=S[2];
         Ave:=Ave+S[2];
         J:=J+1;
         END;
      END;
   Ave:=Ave/(J-1);
   WRITELN(' Set average to 0? ');
   READ(Choice);
   IF Choice='Y' THEN
      FOR I:=1 TO J-1 DO
         BEGIN
         Peak[I]:=Peak[I]-Ave;
         END;
   WRITELN(' Average over 8 samples? ');
   READ(Choice);
   IF Choice='Y' THEN
      BEGIN
      Ave:=0;
      FOR I:=1 TO 8 DO  Ave:=Ave+Peak[I];
      FOR I:=1 TO 302 DO
        BEGIN
        P:=Ave;
        Ave:=Ave-Peak[I]+Peak[I+8];
        Peak[I]:=P;
        END;
      END;
   END;
```

APPENDIX IV. WAVEFORM DIGITIZER

During development of the post-flight data-processing schemes a method of obtaining digitized electric field meter output was required so that the data could be analyzed and appropriate processing algorithms developed. A Hewlett Packard Series 200 desktop computer was used to implement the digital filter synthesis and execution and spectral analysis programs. To digitize analog waveforms an analog-to-digital converter (ADC) was interfaced with the computer. A 10-bit ADC was used, but system noise limited the dynamic range to an equivalent of 8 bits. A block diagram of the system is given in Figure IV.1.

The programmable amplifier gain can be selected by the computer to accommodate signal ranges from 200 mV peak-to-peak up to 40 V peak to peak. The programmable clock controls the sample-and-hold module and the ADC sampling rate as selected by the computer (1 kHz for data presented in this report). The interface performs the transfer of control information and data between the digitizer and the computer.

To digitize a waveform the gain of the amplifier and rate of the clock are first set. The computer detects the end of a sample conversion from the ADC and reads the sample value through the interface. The next sample is read when the end of another sample conversion is detected. This is continued until the desired amount of data is acquired.

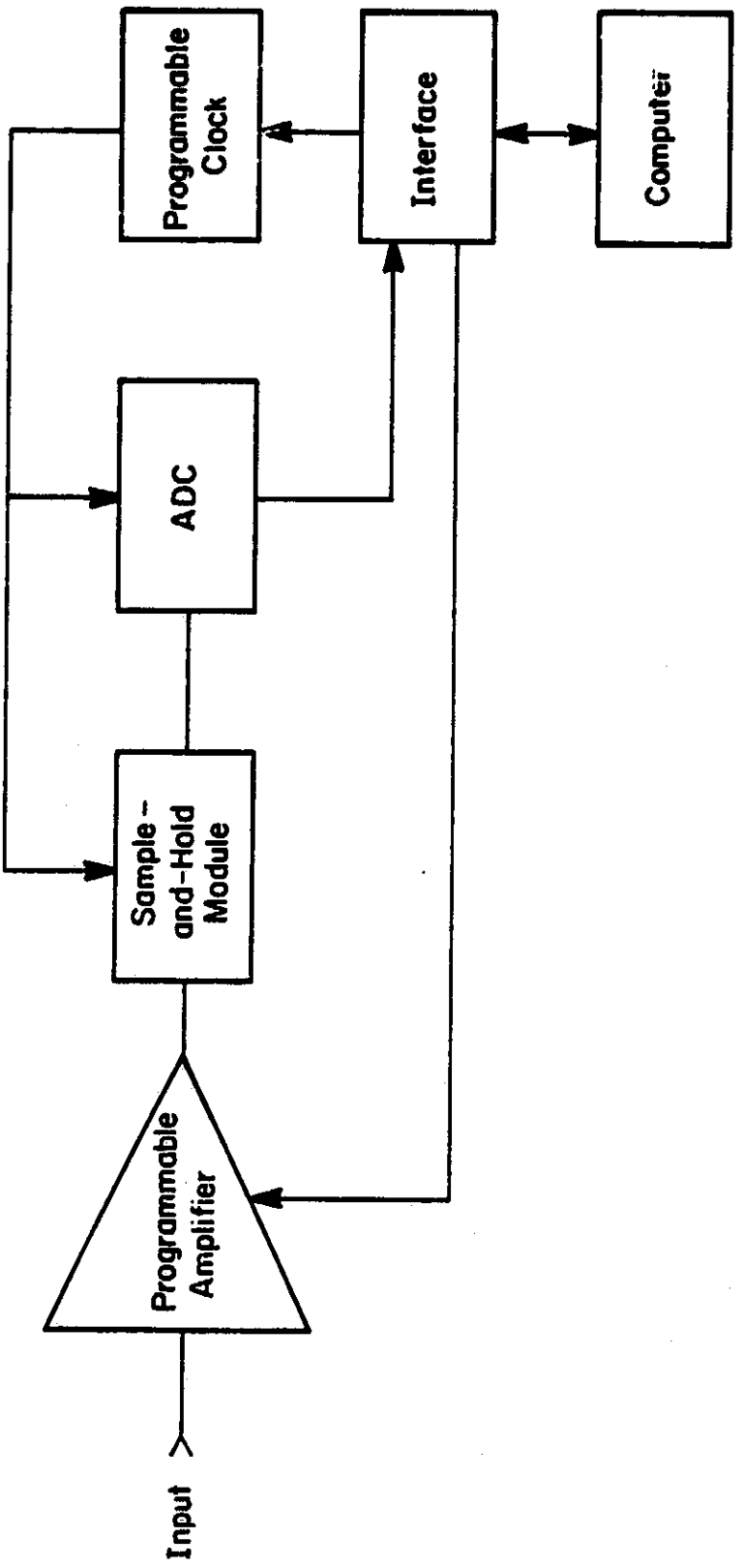

Figure IV.1 Digitizer block diagram.

REFERENCES

Bragin, Y. A., A. A. Tyutin, A. A. Kocheev and A. A. Tyutin [1974], Direct measurement of the atmosphere's vertical electric field intensity up to 80 km, Cosmic Res., 84, 279-282.

Brigham, E. O. [1974], The Fast Fourier Transform, Prentice-Hall, Inc., Englewood Cliffs, New Jersey.

Chalmers, J. A. [1967], Atmospheric Electricity, Pergamon Press, New York.

Dettro, G. L. and L. G. Smith [1982], A rocket-borne electric field meter for the middle atmosphere, Aeron. Rep. No. 105, Aeron. Lab., Dep. Elec. and Comp. Eng., Univ. Ill., Urbana-Champaign.

Elliot, D. F. and K. R. Rao [1982], Fast Transforms: Algorithms, Analyses, Applications, Academic Press, New York.

Gray, P. R. and R. G. Meyer [1977], Analysis and Design of Analog Integrated Circuits, John Wiley and Sons, New York.

Hale, L. C. and C. L. Crosky [1979], An auroral effect on the fair weather electric field, Nature, 278, 239-241.

Hale, L. C., C. L. Crosky and J. D. Mitchell [1981], Measurement of middle-atmosphere electric fields and associated electrical conductivities, Geophys. Res. Lett., 8, 927-930.

Harris, F. J. [1978], On the use of windows for harmonic analysis with the discrete fourier transform, Proc. IEEE, V66, No.1, Jan 1978.

Kelley, M. C., C. L. Siefring, R. F. Pfaff, Jr. [1983], Large amplitude middle atmospheric electric fields: fact or fiction?, Geophys. Res. Lett., 8, 733-736.

Markson, R. [1978], Solar modulation of atmospheric electrification and possible implications for the Sun-weather relationship, Nature, 273, 103-109.

Maynard, N. C., C. L. Crosky, J. D. Mitchell and L. C. Hale [1981], Observations of volt/meter electric fields in the middle atmosphere, Geophys. Res. Lett., 8, 923-926.

Maynard, N. C., F. J. Schmidlin, L. C. Hale and C. L. Crosky [1982], Middle atmosphere campaign: Electric field structure in the high latitude middle atmosphere, EOS Trans., 63, 337.

Mozer, F. S. [1971], Ballon measurements of vertical and horizontal atmospheric electric fields, Pure Appl. Geophys., 84, 32-45.

Oppenheim, A. V. and R. W. Schafer [1975], Digital Signal Processing, Prentice-Hall, Inc., Englewood Cliffs, New Jersey.

Pfaff, R., M. C. Kelley, P. Kintner, C. Cornish, R. Holzworth and L. Hale [1980], Simultaneous measurements of mesospheric and stratospheric electric fields on two rockets and a ballon, EOS Trans., 61, 1056.

Smith, L. G. [1954], An electric field meter with extended frequency range, Rev. Sci. Instr., 25, 510-513.

Taylor, F. J. [1983], Digital Filter Design Handbook, Marcel Dekker, Inc., New York.

Tyutin, A. A. [1976], Mesospheric maximum of the electric field strength, Cosmic Res., 14, 132-133.

Wilson, C. T. R. [1920], Investigations on lightning discharges and on the electric field of thunderstorms, Phil. Trans. A., 221, 73-115.